Catena 242 (2024) 108125

Contents lists available at ScienceDirect

Catena

journal homepage: www.elsevier.com/locate/catena

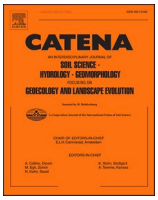

The imprint of coevolving semi-arid landscapes, soil, and vegetation on soil moisture and vegetation variability

Ankur Srivastava [a,b], Omer Yetemen [a,c], Jose F. Rodriguez [a], Nikul Kumari [a,b], Patricia M. Saco [d,a,*]

[a] Centre for Water Security and Environmental Sustainability and School of Engineering, The University of Newcastle, Callaghan 2308, Australia
[b] Faculty of Science, University of Technology Sydney, Sydney, Australia
[c] Eurasia Institute of Earth Sciences, Istanbul Technical University, Maslak 34469, Istanbul, Turkey
[d] Faculty of Engineering & Information Technology, University of Technology Sydney, Sydney, Australia

ARTICLE INFO

Keywords:
Landscape evolution
Soil moisture variability
Vegetation variability
Aspect-driven insolation

ABSTRACT

Landscapes evolve through nonlinear interactions between soil, vegetation, and climate. In semi-arid ecosystems, soil moisture variability (SMV) and vegetation variability (VV) can be strongly related to landscape organisation induced by differences in insolation on opposing north-facing slopes (NFS) and south-facing slopes (SFS). Due to its complex interactions with various processes and factors, soil moisture and vegetation exhibit significant variability in both space and time. In this study, the Channel-Hillslope Integrated Landscape Development (CHILD) landscape evolution model (LEM), coupled to a dynamic vegetation model (BGM) and equipped with a spatially distributed solar radiation component is used. The model is used to investigate the implications of various soil, climatic, and geomorphic factors on SMV and VV over landscapes with different characteristics. The analysis of model results indicates that SMV and VV are more sensitive to changes in geomorphic (hillslope diffusion and uplift rate) and climate (solar radiation, precipitation) factors than to soil hydrologic factors (anisotropy, porosity, infiltration capacity, root depth, and pore size distribution) considered in this study. Spatial variability increases with decreases in hillslope diffusion, and with increases in uplift rates and latitude, while temporal variability has the same response to those factors, and also increases with precipitation. All of these factors contribute to larger difference in condition on NFS and SFS, which ultimately is reflected in SMV and VV. Slope-area, soil moisture-area, and vegetation-area relationships revealed that the difference in SMV and VV between NFS and SFS is more pronounced for smaller contributing areas, where NFS are steeper than SFS. They also show that the temporal variability of soil moisture and vegetation is less in SFS than in NFS.

1. Introduction

Soil-vegetation-topography interactions play a central role in the hydrologic cycle, as well as in the ecological and biogeochemical functioning of a catchment, particularly in semi-arid areas (Istanbulluoglu and Bras, 2006; Gutiérrez-Jurado et al., 2007; Reynolds et al., 2007; Hoekema and Sridhar, 2011; Saco and Heras, 2013; Yetemen et al., 2010, 2015a, 2019; Istanbulluoglu et al., 2012; Baartman et al., 2018; Ding et al., 2018; Rossi et al., 2018; Casalini et al., 2019; Kumari et al., 2019; 2020; Srivastava et al., 2019; 2022). These interactions control numerous processes that are of key importance for water resources problems, including for example evapotranspiration, streamflow regimes, and water-energy connections (Findell and Eltahir, 1997; Detto et al., 2006; Sridhar et al., 2006; Sehgal and Sridhar, 2019; Srivastava et al., 2020). Several biosphere–atmosphere processes are affected by soil moisture and vegetation conditions in semi-arid ecosystems (Pielke et al., 1998; Srivastava et al., 2021). In these ecosystems, a tight coupling between geomorphic processes and hydrological processes exists, which in turn shapes the landscape (Istanbulluoglu and Bras, 2005).

Soil moisture displays substantial spatial and temporal variability, which is modulated by topographic controls and, indirectly, by the geomorphic mechanisms that shape the landscape. It influences a wide range of earth system processes at various spatial and temporal scales (Vinnikov and Robock, 1996; Seneviratne et al., 2010; Evaristo et al., 2015; Dari et al., 2019). Due to its key role in many of these processes,

* Corresponding author.
E-mail address: patricia.saco@uts.edu.au (P.M. Saco).

https://doi.org/10.1016/j.catena.2024.108125
Received 29 October 2023; Received in revised form 6 April 2024; Accepted 22 May 2024
Available online 3 June 2024

numerous recent studies have focused on improving the understanding of the underlying processes governing soil moisture variability (SMV). A deeper understanding of SMV is essential for improving and developing the predictive models of catchment processes, particularly in water-limited ecosystems. Previous studies have shown that a wide variety of factors control the high degree of variability displayed by soil moisture both in space and time. From various modelling and field studies, it has been revealed that SMV is at its maximum when soils are intermediately wet and that it decreases as the soils become wetter or drier (Western et al., 2003; Famiglietti et al., 2008; Ivanov et al., 2010; Srivastava et al., 2021). Many studies have demonstrated that the spatial variability of soil moisture is controlled by factors related to climate, topographic characteristics, vegetation, and soil properties (Nyberg, 1996; Grayson et al., 1997; Vereecken et al., 2007; Martinez et al., 2008; Chen et al., 2014; Yetemen et al., 2015a; Srivastava et al., 2021). For example, Grayson et al. (1997) showed that SMV patterns display two preferred states, with short periods of transition between these states. The first state typically corresponds to dry conditions, when evapotranspiration exceeds precipitation. In this case, the soil moisture pattern reflects the soil and vegetation differences (which control evapotranspiration), and only local terrain influences this pattern. The second state corresponds to wet conditions, when precipitation exceeds evapotranspiration, and topography becomes the dominant factor controlling SMV. However, there can be a combination of several factors which can interact and affect the variability in soil moisture. In their modelling study, Teuling and Troch (2005) demonstrated that spatial vegetation variability (VV) leads to SMV, particularly for dry periods. Similar findings are reported by Teuling et al. (2006) and Pan and Wang (2009).

Vegetation growth is mostly controlled by the amount and availability of soil moisture in space and time (Gutiérrez-Jurado et al., 2013; Zhou et al., 2013; Yetemen et al., 2015a; Srivastava et al., 2019); therefore, soil moisture is an important determinant in vegetation development, particularly in water-limited environments. Further, the shape of the topography at the hillslope or basin scale also affects soil moisture and vegetation distribution (Hack and Goodlett, 1960). Aspect variations and associated solar radiation effects also constitute a characteristic of the topography which affects the development of the vegetation type and density on opposing hillslopes (Yetemen et al., 2015a). These aspect-driven vegetation differences are more profound in water-limited ecosystems, where vegetation growth is limited by soil moisture availability (Gutiérrez-Jurado et al., 2013). The vegetation differences which arise via aspect differences can be seen in different parts of the world, such as in the United States, Australia, Chile, Italy, Spain, and Israel (Kumari et al., 2019; 2020). Modelling efforts by Zhou et al. (2013) revealed that vegetation distribution is controlled by the effect of topographic-driven variations in soil moisture and potential evapotranspiration (PET) at the annual scale in Central New Mexico. Gutiérrez-Jurado et al. (2013) found that solar radiation controls the dynamics of PET and soil moisture across opposing hillslopes. Due to differences in soil moisture, vegetation differences are observed when comparing the vegetation cover and type on opposing hillslopes. These findings illustrate the interdependence between topography, microclimate, soil, and vegetation, which ultimately leads to a complex process of landscape coevolution (Srivastava et al., 2022).

Geomorphic processes define the shape of a landscape, which in turn strongly affects the distribution of soil moisture and vegetation. The association between geomorphic processes and vegetation cover has been addressed in previous studies (Hack and Goodlett, 1960; Istanbulluoglu and Bras, 2006; Gutiérrez-Jurado et al., 2007; Yetemen et al., 2019; Anderson et al., 2013; West et al., 2014; Yetemen et al., 2015a,b). For example, Hack and Goodlett (1960) observed a clear connection between the hydrological, ecological, and geomorphological features of a landscape in Virginia, US. They found that 25 of the 45 vegetation species investigated strongly correlated with the soil moisture and topographic position, slope, and aspect. Several other studies have also shown the relationship between soil moisture and relative elevation, slope, and aspect (Burt and Butcher, 1985; Ding et al., 2018; Srivastava et al., 2021). Additionally, Caylor et al. (2005) showed that topographic features are closely linked to soil moisture distribution.

The shape of the landform is determined by hillslope processes such as fluvial- and diffusion-erosion. The effect of these geomorphic processes can be simulated using landscape evolution models (LEMs) (Tucker and Hancock, 2010; Baartman et al., 2013; Yetemen et al., 2015a; Srivastava et al., 2022). The interaction between hillslope diffusion and fluvial erosion leads to distinct catchment features. As diffusive processes become more dominant (relative to fluvial erosion), drainage density decreases, which in turn can affect soil moisture. Additionally, geomorphic processes such as uplift rate, erosion, and deposition also affect topography through steepness and, therefore, the spatial patterns of SMV and VV. These processes can further be linked to the spatial distribution of vegetation and soil moisture through the slope-area relationship (Willgoose et al., 1991; Perera and Willgoose, 1998; Hancock and Willgoose, 2001), which is the most commonly used geomorphic descriptor to analyze landscape shape and its interactions with ecohydrological processes. Knowledge of landscape development processes is crucial towards understanding landscape evolution, as these processes are integral in determining hillslope geometry, in driving SMV and VV and their response to climate and uplift rate (Carson and Kirkby, 1972; Dietrich et al., 2003). Based on these previous findings, a wide variety of factors can be identified as key drivers of soil moisture and vegetation patterns; however, the role of geomorphic factors (shaping topography) and their interaction with climate, soil, and vegetation factors still remain unclear.

Previous work by Srivastava et al. (2021) used the Bucket Grassland Model (BGM) (Istanbulluoglu et al., 2012) to analyse the effect of several key factors that regulate SMV for two distinct and temporally steady landscape morphologies. The current study examines soil moisture and vegetation variability on coevolving landscapes by considering the role of geomorphic processes, including uplift and hillslope diffusion. The Channel-Hillslope Integrated Landscape Development (CHILD) model (Tucker et al., 2001) and the BGM are used to simulate the evolution of the landscape for 800,000 years. This allows the dynamic vegetation to interact with geomorphic processes, to produce many different coevolving landscape morphologies, which enables a better understanding of the effect of geomorphic factors on SMV and VV. In addition to the effect of geomorphic factors such as hillslope diffusion and uplift rates, the impact of climatic and soil factors on SMV and VV is also investigated. In light of the abovementioned facts, the following research objectives are framed: i) identify the crucial factors that control the spatial SMV and VV in semi-arid ecosystems over long timescales; and ii) examine the association between different factors affecting SMV, VV, and landscape morphology using slope-area, soil moisture-area, and vegetation-area relationships as they can be used to link ecohydrologic and geomorphic processes in different landscapes.

2. Model structure

The coupled CHILD + BGM model is used to investigate the effect of the various factors outlined above for a semi-arid catchment in the Sevilleta National Wildlife Refuge (SNWR) in central New Mexico (Tucker et al., 2001; Istanbulluoglu and Bras, 2005; Yetemen et al., 2015b). The model captures the evolution of the terrain resulting from uplift and fluvial and diffusion processes, and accounts for effects of vegetation on erosion dynamics. Previous studies have used this coupled model for the simulation of geomorphic dynamics (Istanbulluoglu and Bras, 2005; Yetemen et al., 2015a; Srivastava et al., 2022), hillslope asymmetry (Yetemen et al., 2015a), and vegetation effect on landforms (Collin and Bras, 2010).

A description of the CHILD + BGM model is provided below. Modelling details on climate forcing are described first, followed by a description of the formulation used for modelling geomorphic, soil

moisture, and vegetation processes.

2.1. Rainfall forcing

The Poisson rectangular pulse (PRP) rainfall model is modified for incorporation into the CHILD model, in order to generate the stochastic rainfall forcing (Eagleson, 1978). In the model, every storm event is considered to have three essential characteristics: storm intensity (p) [LT^{-1}], storm duration, T_r [T], and inter-storm period, T_b [T]. The mean annual precipitation, (MAP), is expressed as (Collins and Bras, 2010):

$$MAP = \overline{p} \cdot \overline{T_r} \cdot N_s \tag{1}$$

Where $\overline{p}$ and $\overline{T_r}$ represent the mean value of storm intensity and storm duration, and N_s [-] is number of storms in a year, computed as:

$$N_s = \frac{1}{\overline{T_r} + \overline{T_b}} \tag{2}$$

Please note that the values of $\overline{p}$ and $\overline{T_r}$ in this study are selected based on the study regions (for semiarid conditions as explained in more detail the methodology section).

2.2. Geomorphic processes

Geomorphic processes are responsible for sediment transport across a basin. The continuity equation for sediment gives the rate of change in elevation and considers various geomorphic processes (e.g., uplift, hillslope diffusion, and fluvial erosion; Tucker et al., 2001). This can be expressed as follows:

$$\frac{dz}{dt} = U - \nabla . q_d - F \tag{3}$$

where z [L] and t [T] represent elevation and time, respectively. The first term on the right gives the uplift rate, U [LT^{-1}]; the second term states the divergence of volumetric sediment flux per unit width of hillslope diffusion, q_d [LT^{-1}]; and the third term, F [LT^{-1}], provides the fluvial erosion function. The effect of elevation on hillslope diffusion is modelled as (Roering et al., 1999):

$$q_d = \frac{K_d \nabla z}{1 - \left(\frac{|\nabla z|}{S_{cr}}\right)^2} \tag{4}$$

where K_d is diffusivity [L^2T^{-1}] and S_{cr} is the critical hillslope gradient. fluvial erosion, F, is computed as:

$$F = \begin{cases} \nabla q_f, & \text{where } D_c > q_f \\ D_c & \text{elsewhere} \end{cases} \tag{5}$$

where ∇q_f is the net divergence of sediment flux per unit width [LT^{-1}]; and D_c represents the detachment capacity [LT^{-1}], which gives the maximum rate of local erosion. Both detachment (D_c) and transport $\left(q_f\right)$ capacity can be expressed as a power function of shear stress (Meyer-Peter and Müller, 1948; Nearing et al., 1999). The values of D_c and q_f are computed using equations (15) and (16), respectively.

$$D_c = k_d \left(\tau_{eff} - \tau_{cr}\right)^{d_c} \tag{6}$$

$$q_f = k_f \left(\tau_{eff} - \tau_{cr}\right)^{f_c} \tag{7}$$

where k_d and d_c are the detachment-limited erodibility coefficient and exponent, respectively (Nearing et al., 1999); k_f and f_c are the transport-limited erodibility coefficient and exponent, respectively (Meyer-Peter and Müller, 1948); τ_{eff} (Pa) represents the effective shear stress; and τ_{cr} is the critical shear stress for sediment transport. Finally, τ_{eff} is represented with the boundary shear stress and scaled using Manning's roughness coefficient ratio of vegetation (n_v) and bare soil (n_s), following the approach of Laursen (1958) and Istanbulluoglu and Bras (2005):

$$\tau_{eff} = \tau_{bs} \left(\frac{n_s}{n_s + n_v}\right)^{3/2} \tag{8}$$

Roughness due to particular vegetation (n_v) is represented as a power function of its reference vegetation cover, V_R= 0.95, which has a roughness coefficient, n_{vR}= 0.5, as used by Istanbulluoglu and Bras (2005):

$$n_v = n_{vR} \left(\frac{V_t}{V_R}\right)^{\omega} \tag{9}$$

where ω is the parameter that quantifies the relation between vegetation roughness and vegetation cover fraction (V_t).

2.3. Soil moisture dynamics

In CHILD, a water mass balance is kept, and water enters and exits the soil following processes of infiltration, transpiration, evaporation from bare soil, leakage, and lateral soil moisture flux. Soil moisture changes are modelled using a simple bucket model, in which gains are due to infiltration and losses occurs due to leakage and evapotranspiration. The soil water balance in the model is expressed as:

$$\phi Z_r \frac{ds}{dt} = \varphi_a - \chi(s) \tag{10}$$

where ϕ [-] is porosity of the soil, Z_r [L] is the effective root zone depth, s [-] is the ratio of volumetric soil moisture, θ, to the porosity,ϕ, φ_a [LT^{-1}] is the rate of actual infiltration from rainfall, $\chi(s)$ is the rate of soil moisture losses from the soil:

$$\chi(s) = L_t(s) + ET_a(s) \tag{11}$$

L_t [LT^{-1}] and ET_a [LT^{-1}] are the rates of leakage and actual evapotranspiration, respectively. (ET_a estimation, including PET scaling, is detailed in Equation S1 of the Supplementary File). The leakage loss through the soil occurs when the soil moisture content exceeds field capacity, s_{fc}, and is modelled using the approach of Laio et al. (2001):

$$L_t(s) = \begin{cases} K_{sat}, & s = 1 \\ K(s) = K_{sat} s^{\beta}, & s_{fc} < s \leq 1 \end{cases} \tag{12}$$

where K_{sat} [LT^{-1}] is saturated hydraulic conductivity and $K(s)$ [LT^{-1}] is unsaturated hydraulic conductivity, respectively, β is pore size distribution. Total Leakage $\left(L_t = L_v + L_p\right)$ is divided into lateral (L_p) and vertical (L_v) components which depends on topographic gradient and soil properties. Lateral soil moisture transfer, L_p, in the direction parallel to the surface is computed as (Cabral et al., 1992):

$$L_p = L_t \left(\frac{A_r \tan S}{1 + A_r \tan S}\right) \tag{13}$$

where A_r [-] is anisotropy ratio, the ratio of horizontal saturated hydraulic conductivity to the vertical one, S [L/L] is surface gradient. The vertical component of the leakage which is trivial compared to L_p in highly anisotropic medium is computed as $L_v = 1 - L_p$.

Both infiltration and saturation excess runoff are included in the model. Local runoff occurs where the sum of local rainfall rate and the run-on discharge from upstream cells, routed along connected flowpath cells, exceeds the infiltration capacity. Storage excess runoff occurs when the soil saturates during a rainfall event and thus any rain after that becomes surface runoff. Hence, φ_a is limited by three factors: the rate of water flux, infiltration capacity, and the available pore space in the root zone. In semi-arid ecosystems, the majority of the runoff is generally produced by the infiltration excess runoff mechanism (Collins et al., 2010), and the infiltration capacity is, therefore, the dominant factor for infiltration in this case. The infiltration capacity, φ_{cap} [LT^{-1}],

is dependent on vegetation cover (Dunne et al., 1991):

$$\varphi_{cap} = \varphi_{cap,bare}(1 - V_t) + \varphi_{cap,veg} V_t \quad (14)$$

where $\varphi_{cap,bare}$ and $\varphi_{cap,veg}$ are respectively bare soil infiltration capacity and fully-vegetated surface infiltration capacity, and V_t is [-] vegetated surface fraction.

2.4. Vegetation dynamics

The role of vegetation in shaping landforms and the effect of various factors on landform organisation are also analysed. Soil moisture and vegetation dynamics in CHILD are simulated for grass using a single layer bucket model which represents uniform soil moisture within the root zone and are distributed spatially using laterally connected elements in the direction of flow. Each model cell is covered by grass (live and dead) and bare soil fractions, which are updated following every storm event. The net primary productivity (NPP) of grass biomass (g/m^2) is calculated as a function of interstorm evapotranspiration and water use efficiency (WUE) and then allocated to aboveground and belowground biomass compartments (Swenson and Waring, 2006), as follows:

$$NPP = 0.75 \cdot (1 - \mu) \cdot ET_a \cdot WUE \cdot \rho_w \cdot \omega \quad (15)$$

where μ is the ratio of exchange of CO_2 from daytime to nighttime, ρ_w is the density of water (kg/m^3), and ω is a conversion factor of CO_2 to dry biomass (kg DM/kg CO_2). The production of the sum of above-ground and below-ground grass biomass at the ecosystem scale is related linearly with ET_a through the use of water use efficiency, WUE, (ratio of biomass produced by plants to the amount of water transpired by a plant). The vegetation cover fraction, V_t [-], for total biomass is represented by an exponential function, following Lee (1992):

$$V_t = [1 - \exp(-0.75 \cdot LAI_t)] \quad (16)$$

where the leaf area index LAI_t includes green and dead biomass.

3. Methodology

3.1. Study area and model calibration

As mentioned before, the model is used to simulate conditions found at the Sevilleta National Wildlife Refuge (SNWR) site in central New Mexico (Yetemen et al., 2015b). SNWR is a semi-arid site with extensive data availability, and the model used in the current study (i.e., CHILD + BGM) has previously been calibrated and validated for this site using observed runoff, soil moisture content in the top 30 cm, actual evapotranspiration, and leaf area index (LAI) from the Moderate Resolution Imaging Spectroradiometer (MODIS) (Yetemen et al., 2015a). The SNWR has an annual rainfall of 250 mm, with almost 50 % of the rainfall occurring during the North American Monsoon (NAM) season (i.e., from July to September). The soil texture is loamy sand, with vegetation type consisting of grass with a root depth of 30 cm. Results from the simulated landscape morphology are tested in Yetemen et al., (2015a) using drainage density and hillslope asymmetry (HA) indices as the metrics to provide objective comparisons between modelled and actual field catchments. These metrics showed that the simulated landform patterns are consistent with the observed patterns, confirming that the model is capable of capturing the geomorphologic characteristics of the study site (Yetemen et al., 2015a).

The current study uses the calibrated soil and vegetation parameters from this previous work of Yetemen et al., (2015a,b). The calibrated model is used to run simulations over a period of 800,000 years using an initial synthetic domain of 900 x 900 m (20 x 20 m resolution), with elevations ranging between 0 and 67 m, and drainage only permitted through a single side of the domain (as shown in Fig. 1).

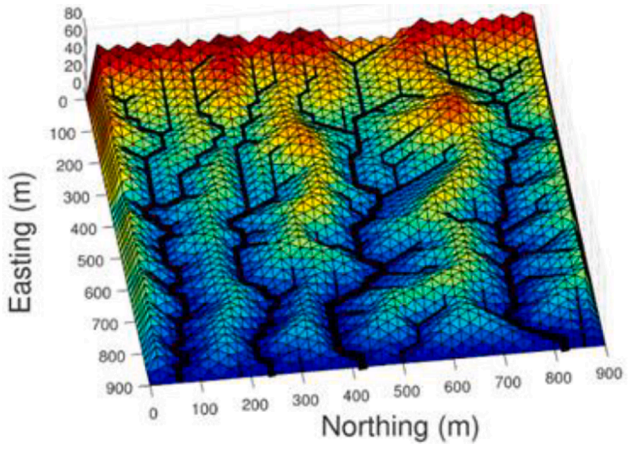

Fig. 1. Elevation map of modelled landscape morphology used in the design of the CHILD + BGM numerical experiments to analyse the SMV and VV (control scenario described in Table 1). The channels are generated using 2000 m^2 as a threshold area.

3.2. Numerical model settings

A total of 38 simulations using the CHILD + BGM model are run for 800,000 years, to enable sufficient time for the simulated landscapes to reach uplift-erosion equilibrium. The simulations are designed to analyse the effect of different factors which affect soil moisture, and how this response is conditioned by the vegetation and climate under which landscapes coevolve.

Model simulations are designed to assess the effect of different key factors on SMV and VV (i.e., aspect, latitude, hillslope diffusivity, uplift, spatially uniform precipitation, elevation control on precipitation, anisotropy in hydraulic conductivity, porosity, pore-size distribution, infiltration rate, and root-zone depth). The parameters reported by Yetemen et al., (2015a) for both vegetation and geomorphic dynamics are used in this analysis for the control scenario (Table 1). The effect of the different factors known to modulate vegetation and soil moisture dynamics, is investigated by modifying the value of some key

Table 1
List of control factors and range of parameter values used to explore their effect on SMV and VV.

Factors	Control Scenario	Other Scenarios
Aspect	Slope control on radiation	Uniform radiation
Latitude	34°N	15°N; 30°N; 45°N
Hillslope diffusion	0.003 m^2/y	0.0003 m^2/y; 0.0090 m^2/y; 0.0150 m^2/y
Uplift rate	0.1 mm/y	No uplift; 0.05 mm/y
Spatially uniform mean annual precipitation (*MAP*)	250 mm	200 mm; 300 mm; 400 mm; 500 mm; 600 mm
Elevation control on MAP	250 mm	250–300 mm; 250–350 mm; 250–400 mm; 250–450 mm; 250–500 mm
Anisotropy (A_r)	1	0.001; 0.01; 0.1; 10; 100; 1000
Porosity (ϕ)	0.420	0.342; 0.410; 0.478
Infiltration capacity (I_c)	Bare soil: 12 mm/hr; Vegetated soil: 36 mm/hr	Bare soil: 12 mm/hr and Vegetated: 12 mm/hr; Bare soil: 36 mm/hr and Vegetated: 36 mm/hr
Root zone depth (Z_r)	0.3 m	0.2 m; 0.4 m; 0.5 m
Pore size distribution (β)	12.7	8.82; 11.76; 14.70

Note: Factors used in the control scenario (second column of Table 1) correspond to those obtained from the calibration of the CHILD + BGM model for the SNWR study site in central New Mexico. This scenario is used as a reference for the comparison of SMV and VV among all scenarios on coevolving landforms.

parameters as shown in Table 1, which displays the parameters used in the simulations. The rationale for parameter selection is explained in detail below, and the choice/range of values was selected based on values reported in the literature (as explained in more detail below).

The role of solar radiation in the spatial and temporal distributions of vegetation and soil moisture, is investigated by including changes in aspect and latitude. Two different scenarios are designed to investigate this effect: i) slope control on radiation and ii) uniform radiation. For the slope control radiation case, solar radiation is spatially and temporally varied as a function of day of year, latitude, aspect, and slope throughout the domain. For the uniform radiation, solar radiation is assumed uniformly distributed over the domain as a function of day of year and latitude. In this last scenario, every cell in the model domain receives an amount of solar radiation corresponding to that of a flat surface on that day. Latitude is a major factor for the availability of water as energy changes with the latitudinal variation of solar radiation. The role of latitude on SMV and VV is investigated for four scenarios with latitudes of 15°N, 30°N, 34°N, and 45°N.

Geomorphic effects on SMV and VV are studied for different equilibrium landscapes obtained under coevolving dynamic vegetation effects and different diffusion and uplift rates. The relative dominance of diffusive and fluvial drivers was investigated through changes in the following parameters: i) the hillslope diffusivity coefficient (K_{diff}) and ii) the uplift rate. The effect of hillslope diffusivity was explored by generating four different synthetic landscapes (Fig. 2) obtained using diffusion coefficients ranging from low $K_{diff} = 0.0003$ m^2/y to high $K_{diff} = 0.0150$ m^2/y (Fig. 2). Hillslope diffusivity modulates the amount of dissection of a landscape by the channel network, which is also governed by a range of factors including climate, erosion rate, and hillslope morphology, and the roughness of the topographic surface (Dunne et al., 1991; Thompson et al., 2010). Landscapes with longer and smoother hillslopes result from the dominance of hillslope diffusion, which affects flow accumulation (or contributing area) as also shown in Fig. 2.

Uplift rate modulates topographic steepness, which in turn affects the distribution of solar radiation on hillslope elements. The role of uplift rate on SMV and VV is explored for three different cases (no uplift, low uplift rate [0.05 mm/y], and high uplift rate [0.10 mm/y]), as illustrated in Fig. 3 (a-c). These uplift rates are within the ranges of the long-term (~640 ka) average incision and denudation rate previously estimated for this region (Dethier, 2001). The joint effect of uplift, diffusion and fluvial erosion over time leads to dynamic equilibrium conditions. CHILD is forced with an uniform uplift rate obtained by averaging the erosion estimates from the study site. The hillslope diffusion and uplift rates considered in the current model are described in equations (3)–(5) of Section 2.2.

Investigating how differences in precipitation influence landscape evolution can help to infer how landscapes may change in the future under different climate conditions. Model simulations are performed with six different mean annual precipitation (MAP) scenarios to evaluate the impact on SMV and VV. MAP scenarios were chosen to represent a range of conditions from a dry-climate state (MAP = 200 mm) to a wet climate state (600 mm) for a semi-arid region, such as the one considered here. The input rainfall time series for each different MAP value is obtained using a random distribution model (as shown in Equation (1) and (2) that simulates rainfall events for the Southwestern US (Small, 2005) so that, for example, the MAP = 600 mm scenario has more frequent and intense storms compared with the MAP = 200 mm scenario (Srivastava et al., 2022). The effect of elevation on rainfall is simulated using a linear orographic precipitation model for its simplicity and ability to represent the observed patterns in the Southwestern US (Osborn, 1984; Wainwright, 2005; Nearing et al., 2015; Srivastava et al., 2021; 2022), in which the precipitation is scaled linearly as a function of elevation. Details on how MAP was incorporated in the model used for this study are provided through equations (1)–(2) in Section 2.1.

Various studies have shown that soil properties such as porosity (ϕ) and anisotropy in hydraulic conductivity (A_r) are key drivers of SMV (Famiglietti et al., 1998; Vereecken et al., 2007), and can also affect landform shape and surface and subsurface processes (Ivanov et al., 2008; Yetemen et al., 2015a; Ding et al., 2018). Additionally, in water-limited ecosystems, vegetation growth is highly influenced by the soil's water holding capacity as the distribution and size of pores within the soil directly influence its ability to retain and store water (Geroy et al.,

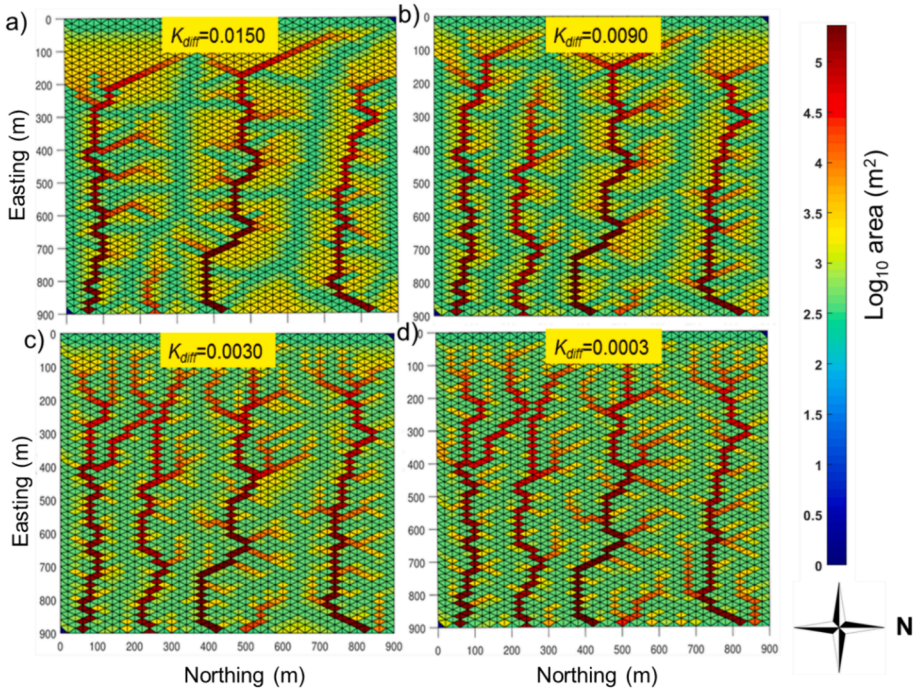

Fig. 2. Plan views of the four different landscapes used obtained from the numerical experiments designed to investigate the role of hillslope diffusivity. a) K_{diff} = 0.0150 m^2/y, b) K_{diff} = 0.0090 m^2/y, K_{diff} = 0.0030 m^2/y, and d) K_{diff} = 0.0003 m^2/y. The colour scheme depicts the magnitude of the drainage area contributing to each cell.

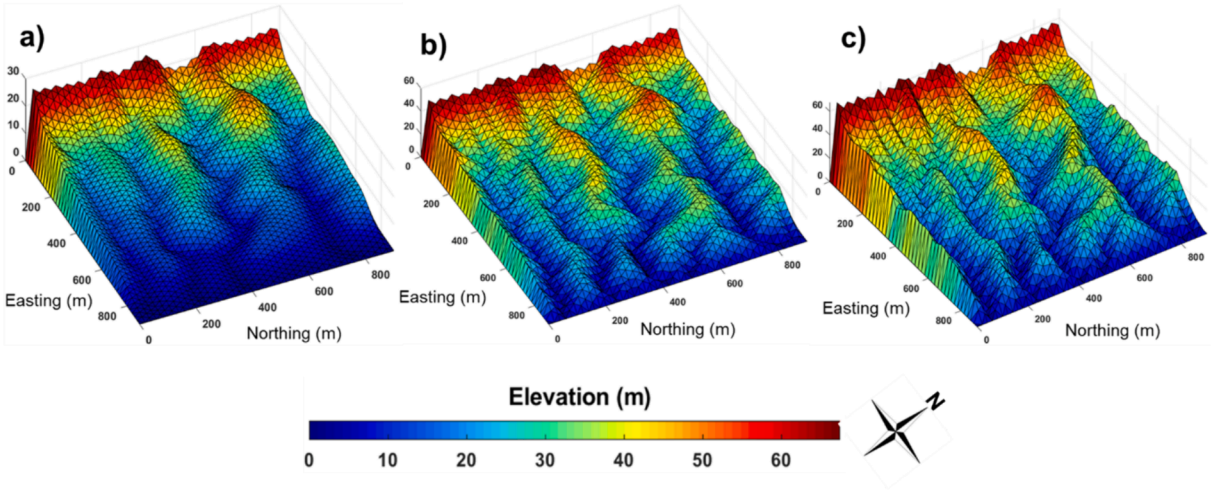

Fig. 3. Simulated elevation maps for the three uplift scenarios used in the numerical experiments. a) No uplift (U = 0 m/y), b) medium uplift (U = 0.05 mm/y), and c) high uplift (U = 0.1 mm/y).

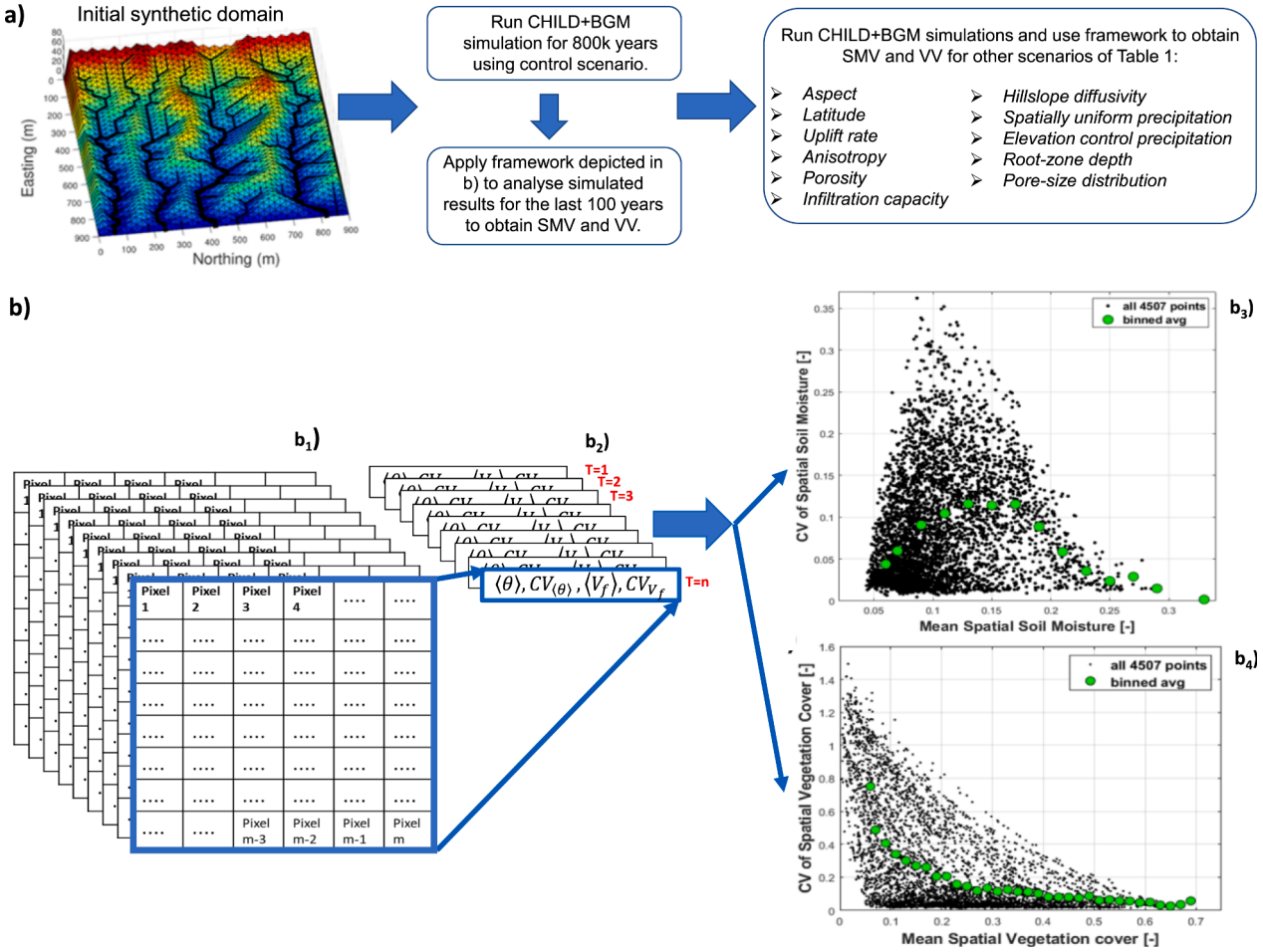

Fig. 4. Methodology for the assessment of the effects of soil, climatic, and geomorphic factors on SMV and VV on coevolving landscapes. a) flow chart indicating the steps in the computations of SMV and VV; b) framework used to compute spatial soil moisture and vegetation variability. b_1) modelled soil moisture and vegetation cover values from m (1936) pixels and n (4507) time steps; b_2) computation of mean spatial soil moisture $\langle\theta\rangle$, CV of spatial soil moisture $CV_{\langle\theta\rangle}$, mean spatial vegetation cover $\langle V_f\rangle$ and CV of spatial vegetation cover CV_{V_f} for each time step; b_3) $CV_{\langle\theta\rangle} - \langle\theta\rangle$ plotted for all time steps (black dots) and binned averaged values (green dots) obtained from the soil moisture simulations (shown here for the control scenario); and b_4) $CV_{V_f} - \langle V_f\rangle$ plotted for all time steps (black dots) and binned averaged values (green dots) obtained from the vegetation simulations (shown here for the control scenario). (For interpretation of the references to colour in this figure legend, the reader is referred to the web version of this article.)

2011). Therefore, variations in the water holding capacity not only directly affect SMV but can also trigger feedbacks that can further affect the resulting SM patterns. To investigate how these two factors drive SMV and VV, simulations are performed using a range of values from a lower anisotropic ($A_r = 0.001$) to a highly anisotropic ($A_r = 1000$) soils, and from low porosity ($\phi = 0.342$) to high porosity ($\phi = 0.478$) soils. The mean of the observed porosity values (ϕ) reported in the literature for loamy sand is 0.410, with a standard deviation of 0.068 (Clapp and Hornberger, 1978).

Local-scale variations in vegetation significantly affect SMV due to its effect on infiltration and root water uptake. Consequently, changes in infiltration capacity and root depth are also included in the current analysis. Field studies have shown that infiltration rate beneath plant canopies is higher than in intercanopy areas (e.g., Bhark and Small, 2003). Hence, water recharge in the root zone and runoff production on the surface are modified by infiltration rates (Saco and Moreno de las Heras, 2013; Rossi et al., 2018). As a major consumer of soil moisture in semi-arid ecosystems, plants modify root-zone soil moisture through root water uptake. The increased availability of soil moisture in deeper soils can promote more vegetation cover on the surface and may increase the survival chance of vegetation during a drought period. The implications of varying infiltration capacities (between bare and vegetated areas) are explored with different scenarios, as shown in Table 1. A 30-cm root depth is used in the control scenario, but to assess the influence of this factor on SMV, values ranging from 20 to 50 cm are also investigated.

The impact of variations in soil water retention on SMV can be investigated by modifying the shape parameter of the van Genuchten-Mualem model (van Genuchten, 1980). The effect of the shape parameter is captured by modifying the pore size distribution (β) on the Brooks-Corey model, which correlates with the soil's clay content (Famiglietti et al., 1998; Vereecken et al., 2007) and affects the shape of the entire moisture retention capacity (particularly in the moisture range where most SMV occurs). In the current study, β values are selected following the study of Laio et al. (2001) (shown in Table 1).

3.3. Method of analysis

The variability of the spatial patterns of soil moisture and vegetation cover fraction are computed and analysed following an approach similar to that presented in Srivastava et al. (2021), adapted to include the effect of coevolution (Fig. 4). As explained previously, CHILD + BGM is run for 800,000 years using a rainfall input over the entire synthetic domain generated stochastically (as explained in section 2.1), and the last 100 years of simulated soil moisture and vegetation cover are extracted for the spatial variability analysis (Fig. 4a). The spatial variability is analysed using the approach displayed in Fig. 4b for the control scenario and discussed below. Fig. 4b1 represents the simulated soil moisture (and vegetation) data over the entire domain (including 1936 pixels) and the entire 100-year time-period (4507 time steps). To analyse the variability of soil moisture (and vegetation) over time, values of mean spatial soil moisture $\langle\theta\rangle$, coefficient of variation of soil moisture $CV_{\langle\theta\rangle}$, mean spatial vegetation cover $\langle V_f\rangle$ and coefficient of variation of vegetation cover CV_{V_f} for each time step are computed using all cells in the synthetic domain (as illustrated in Fig. 4b2). The mean spatial variance of soil moisture and vegetation cover fraction are computed first to estimate the respective coefficients of variation $CV_{\langle\theta\rangle}$ and CV_{V_f}. The black dots shown in Fig. 4b3 display the values of $CV_{\langle\theta\rangle}$ as a function of $\langle\theta\rangle$. Results from all time steps are binned (using $\langle\theta\rangle$ intervals of 0.02) to obtain a clearer trend (green dots in Fig. 4b3) suitable for comparison with previous results (Ivanov et al., 2010; Yetemen et al., 2015a; Srivastava et al., 2021). Similarly, the black dots in Fig. 4b4 display the values of CV_{V_f} versus $\langle V_f\rangle$. The same approach was used to compute $\langle\theta\rangle$, $\langle V_f\rangle$, $CV_{\langle\theta\rangle}$ and CV_{V_f} for other scenarios detailed in Table 1. In addition to the previous values and to capture the variability of the soil moisture in space (including areas with different aspects), the mean value of soil moisture and vegetation cover are computed for each pixel over the entire period. These values are referred to as mean temporal soil moisture $\overline{\theta}$ and mean temporal vegetation cover $\overline{V_f}$, respectively.

4. Results and discussion

4.1. Spatial variability of soil moisture

The spatial variability of soil moisture is investigated by analyzing the relationship between $\langle\theta\rangle$ and $CV_{\langle\theta\rangle}$ for all controlling factors. The analysis showed that only four of the factors (solar radiation, latitude, hillslope diffusion, and uplift rate) had an effect on the spatial SMV (Fig. 5), while variability on the other factors (using the range of parameters displayed in Table 1) showed negligible differences in SMV (Figure S1 in Supplementary File).

As explained in section 3 and displayed in Fig. 5, the outcomes for each time step have been binned into intervals of 0.02 to improve the visualization of soil moisture patterns, providing a clearer picture of the spatiotemporal trends. A convex shape for the $CV_{\langle\theta\rangle} - \langle\theta\rangle$ relation is obtained from the simulated soil moisture values for all factors, such that the maximum spatial variance occurs at mid-values of $\langle\theta\rangle$. Furthermore, the dry end of $\langle\theta\rangle$ corresponds to the domain of hygroscopic water content and the permanent wilting point values (~0.04–0.07), while the wetter end falls within the domain of field capacity and porosity values (~0.22–0.42). This $CV_{\langle\theta\rangle} - \langle\theta\rangle$ relationship is consistent with previous studies reported in the literature (Famiglietti et al., 1999; Western et al., 2003; Ryu and Famiglietti, 2005; Wang et al., 2017; Fan et al., 2019; Ivanov et al., 2010; Yetemen et al., 2015a).

Fig. 5a shows the coefficient of the spatial variation of soil moisture plotted as a function of mean spatial soil moisture for the two radiation scenarios. Higher spatial variability in soil moisture can be observed for the slope control solar radiation case compared with the uniform solar radiation case. The maximum value of $CV_{\langle\theta\rangle}$ for slope control radiation reaches ~ 0.13, which falls between the stomatal closure value (θ^*) and field capacity (θ_{fc}); however, for the case considering uniform solar radiation, there is no obvious range of soil moisture content that maximizes $CV_{\langle\theta\rangle}$. The considerable variation in $CV_{\langle\theta\rangle}$ of the slope control radiation can be attributed to the control of aspect and slope on solar radiation, and its effect on evapotranspiration in semi-arid regions. Fig. 5b displays the spatial variation of soil moisture as a function of the mean spatial soil moisture for the four different latitudes analysed (i.e., 15°N, 30°N, 34°N, and 45°N). The plot shows that the 45°N latitude exhibits the highest $CV_{\langle\theta\rangle}$ compared to the remaining three latitudes. The $CV_{\langle\theta\rangle}$ reaches a maximum in the intermediate range (~0.13) of the soil moisture values for all latitudes. The variability in spatial soil moisture increases from lower (15°N) to higher (45°N) latitudes. This trend can be also explained by changes in solar radiation, which in this case are due to the effect of latitude. For different latitudes, the availability of water and energy changes as the global distribution of solar radiation varies from the equator to higher latitudes (Gerten, 2013), that highlights the effect of latitude on SMV(Yetemen et al., 2015b; Kumari et al., 2020; Srivastava et al., 2021).

Fig. 5c shows the geomorphic effect of the landscape morphologies obtained using four different hillslope diffusion parameters, ranging from 0.0003 m^2/y to 0.015 m^2/y on the $CV_{\langle\theta\rangle} - \langle\theta\rangle$ plot. The $CV_{\langle\theta\rangle}$ for the case $K_{diff} = 0.0003$ m^2/y reaches a maximum at intermediate values of $\langle\theta\rangle$= ~0.10, while for the remaining three K_{diff} cases, $CV_{\langle\theta\rangle}$ reaches a maximum at $\langle\theta\rangle$= ~0.17. It can be also observed that the highest spatial variability in soil moisture occurs for the lowest K_{diff} case (0.0003 m^2/y) and the lowest spatial variability in soil moisture is achieved for the highest K_{diff} case (0.0150 m^2/y). This can be attributed to the fact that landscapes with dominant diffusive erosion processes (K_{diff} = 0.0090 and 0.0150 m^2/y) are relatively more uniform as observed from the four different synthetic landscapes created by varying the hillslope diffusion

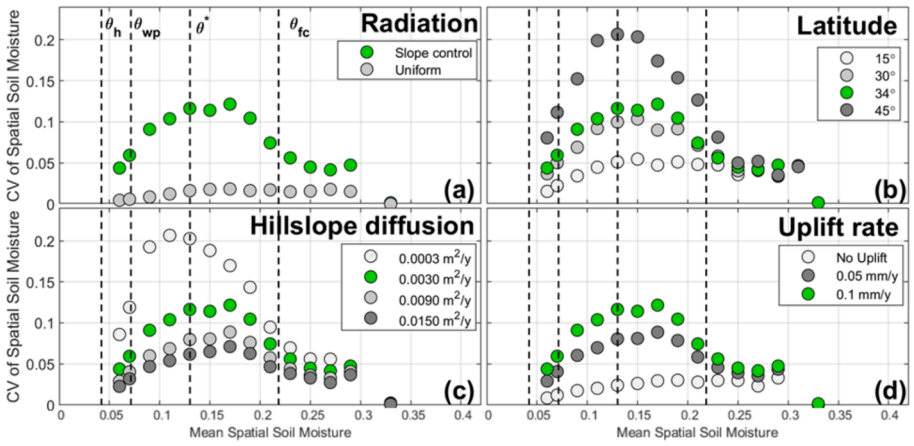

Fig. 5. Coefficient variation of spatial soil moisture content ($CV_{\langle\theta\rangle}$) plotted as a function of mean spatial soil moisture $\langle\theta\rangle$ over the entire domain for four different soil moisture controlling factors (a–d). The $\langle\theta\rangle$ results for each time step are binned and plotted against $CV_{\langle\theta\rangle}$. The dashed lines represent the different soil moisture states. hygroscopic water content ($\theta_h = 0.04$), plant wilting point ($\theta_w = 0.07$), incipient stomata closure ($\theta^* = 0.13$), and field capacity ($\theta_{fc} = 0.22$) for the loamy sand soil (porosity = 0.42) used in the simulations. The green symbols represent the control simulations detailed in Table 1. (For interpretation of the references to colour in this figure legend, the reader is referred to the web version of this article.)

and shown in Fig. 2. Landscapes that have a relatively higher spatially varibility and higher drainage density, found in fluvial-dominated domains result in larger spatial variability in soil moisture. Fig. 5d shows the results of $CV_{\langle\theta\rangle} - \langle\theta\rangle$ for the three different uplift cases (0 mm/y, 0.05 mm/y, and 0.1 mm/y) used in this study. The uplift case of 0.1 mm/y results in the highest spatial SMV, whereas the no uplift case has the lowest spatial SMV (also shown in Figure S2 of the Supplementary File). The $CV_{\langle\theta\rangle}$ reaches a maximum in the intermediate range (~0.17) of soil moisture values for all three uplift cases used. This is due to uplift affecting topographic steepness, which in turn affects the distribution of solar radiation on hillslope elements. The increase in SMV in response to 0.1 mm/y can be attributed to the enhancement of the insolation difference between NFS and SFS due to greater uplift rates (Yetemen et al., 2015a).

In order to analyse more general trends in SMV integrating both space and time, the $\overline{CV_{\langle\theta\rangle}}$ (i.e., the value obtained as the mean of the time series of $CV_{\langle\theta\rangle}$) was computed as a function of $\overline{\langle\theta\rangle}$ (i.e., mean of $\langle\theta\rangle$) for different soil moisture controlling factors and plotted in Fig. 6. Latitude, hillslope diffusion and MAP are used to analyse the overall trends in $\overline{CV_{\langle\theta\rangle}}$ *versus* $\overline{\langle\theta\rangle}$. As seen in Fig. 6, the observed trends can be classified

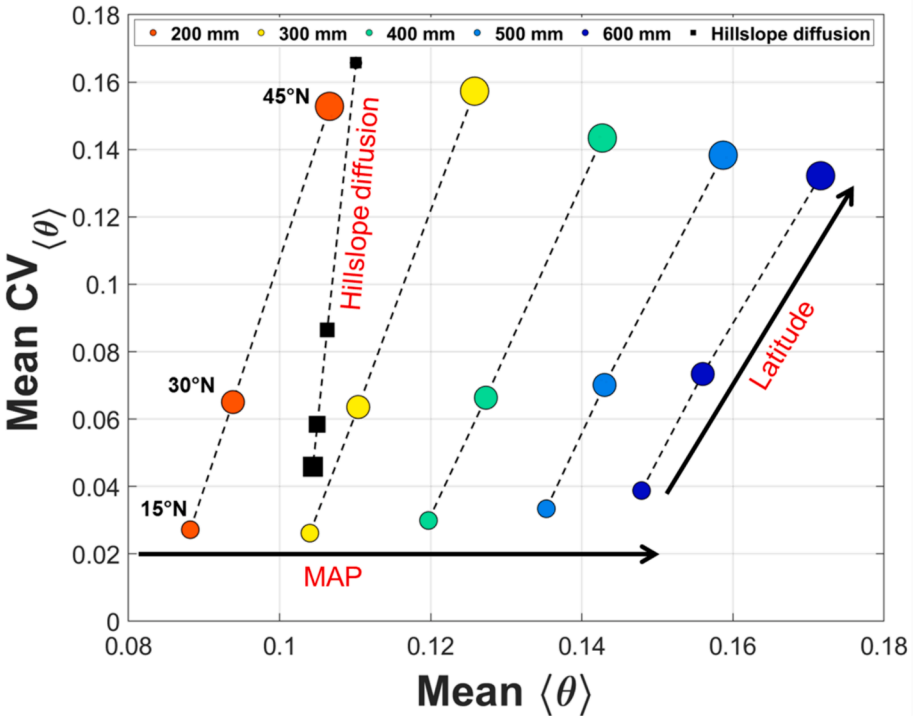

Fig. 6. $\overline{CV_{\langle\theta\rangle}}$ plotted as a function of $\overline{\langle\theta\rangle}$ over the entire domain for the selected soil moisture controlling factors. Five different MAP scenarios (represented by the different coloured circles) at three different latitudes (represented by the different circle sizes) and three different hillslope diffusion scenarios (represented by the different square sizes) are shown. The smaller circle sizes represent latitude 15°N, the medium size is 30°N, and the larger size is 45°N, obtained for $K_{diff} = 0.003$ m^2/y. The larger square represents the highest value of $K_{diff} = 0.0150$ m^2/y and the smaller one represents the lowest $K_{diff} = 0.0003$ m^2/y. Note that the hillslope diffusion case is shown for a MAP of 250 mm and a latitude of 34°N.

into three different types: i) change in $\overline{\langle\theta\rangle}$ (increase in the x direction) without change in $\overline{CV_{\langle\theta\rangle}}$; ii) change in $\overline{CV_{\langle\theta\rangle}}$ (increase in the y direction) without substantial change in $\overline{\langle\theta\rangle}$; and iii) increase in both the $\overline{\langle\theta\rangle}$ and $\overline{CV_{\langle\theta\rangle}}$ (increase in both the x and y direction). Fig. 6 shows that for changes in MAP at a given latitude, the $\overline{\langle\theta\rangle}$ increases but the $\overline{CV_{\langle\theta\rangle}}$ does not show large variations, with the values for a latitude of 15° slightly increasing while the values for 45° slightly decreasing. Each increment of 100 mm in MAP results in an increase of ~ 0.015 in $\overline{\langle\theta\rangle}$. The second trend illustrated in Fig. 6 shows the effect of changes changing K_{diff}, which has a significant impact on $\overline{CV_{\langle\theta\rangle}}$, but it does not affect the $\overline{\langle\theta\rangle}$ when constant values of MAP and latitude are considered. These results indicate that the variability is higher for the lowest hillslope values of diffusion, K_{diff} (0.0003 m^2/y) due to the denser channel network, higher drainage density and dissections (as shown in Fig. 2), which in turn lead to steeper NFS than SFS (Srivastava et al., 2021).

The last trend with variations in both directions (i.e., an increase in $\overline{\langle\theta\rangle}$, as well as in $\overline{CV_{\langle\theta\rangle}}$) is obtained when considering the effects of latitude and precipitation. It can be observed in Fig. 6 that a MAP of 400 mm at a latitude of 45°N leads to wetter soil moisture values than those obtained for a MAP of 500 mm at a latitude of 15°N. For the equal values of MAP, the $\overline{CV_{\langle\theta\rangle}}$ values at latitude 45°N are eight times greater than those at latitude 15°N. For example, the $\overline{CV_{\langle\theta\rangle}}$ value for MAP = 400 mm at 45°N is ~ 0.14, while at 15°N, the $\overline{CV_{\langle\theta\rangle}}$ value is ~ 0.02. Towards the higher latitude (45°) for all MAP values (i.e., 200, 300, 400, 500, and 600 mm), the $\overline{CV_{\langle\theta\rangle}}$ value rises significantly. This occurs because soil moisture at any latitude is driven by aspect-controlled solar radiation, which increases with increasing latitude, from 15°N to 45°N (Gutiérrez-Jurado et al., 2013; Yetemen et al., 2015a; Srivastava et al., 2021). The combined effect of MAP and latitude also produces a pattern of decreasing $\overline{CV_{\langle\theta\rangle}}$ with increasing MAP for the higher latitudes, but a slightly increasing trend of $\overline{CV_{\langle\theta\rangle}}$ with increasing MAP for the lower latitudes. This different behaviour can be associated with high differences between NFS and SFS radiation conditions for the high latitudes that get gradually smoothed out by higher values of precipitation (and soil moisture), whereas the slight increase in $\overline{CV_{\langle\theta\rangle}}$ might be due to larger effects of temporal variability for larger values of MAP, as differences between NFS and SFS are not important. Interestingly, extrapolation of the trends of $\overline{CV_{\langle\theta\rangle}}$ for large MAP and $\overline{\langle\theta\rangle}$ and for the different latitudes shows a convergence towards a value of $\overline{CV_{\langle\theta\rangle}}$ of about 0.09, which is about twice the asymptotic value of the spatial coefficient of variability $CV_{\langle\theta\rangle}$ (Fig. 5b). Because $\overline{CV_{\langle\theta\rangle}}$ includes both temporal and spatial variability, this would indicate that the temporal variability for high values of soil moisture is of about the same magnitude as the spatial variability.

4.2. Spatial variability of vegetation

This section shifts the focus to understanding how different factors affect the spatial variability of vegetation cover. Fig. 7 shows the relationship between CV_{V_f} and $\langle V_f\rangle$ after binning the last 100 years duration obtained from model simulations. It is important to note that $\langle V_f\rangle$ represents the mean spatial vegetation cover state in response to the MAP of 250 mm (except for Fig. 7e and 7f). It can be observed from the $CV_{V_f} - \langle V_f\rangle$ relationship that the lowest CV_{V_f} is observed at the wet end, with high $\langle V_f\rangle$; whereas, the highest CV_{V_f} occurs for low $\langle V_f\rangle$ for all cases except uniform radiation (Fig. 7a).

Results for $CV_{V_f} - \langle V_f\rangle$ for the slope-controlled solar radiation and uniform solar radiation scenarios are shown in Fig. 7a. Slope-controlled radiation displays the highest spatial variability in vegetation cover, with a maximum value of CV_{V_f} = ~0.8, while uniform radiation reveals an almost negligible variation in CV_{V_f}. This behaviour can be attributed to the aspect and slope controls on solar radiation, which play a vital role in influencing vegetation distribution. The higher CV_{V_f} is due to the difference in insolation between the NFS and SFS, which is intensified for low $\langle V_f\rangle$ values. Solar radiation plays a key role in the spatial distribution of vegetation due to its impact on soil moisture (Gutiérrez-Jurado et al., 2007; Martinez et al., 2008; Bass et al., 2017; Yetemen et al., 2015a; Srivastava et al., 2019; Srivastava et al., 2021).

The comparison of the $CV_{V_f} - \langle V_f\rangle$ relationship from simulations for the four different latitudes used in the study (i.e., 15°N, 30°N, 34°N, and 45°N, Fig. 7b) reveals that the highest latitude (i.e., 45°N) exhibits the highest CV_{V_f} compared with the remaining three latitudes for $\langle V_f\rangle$ up to ~ 0.3. Thereafter, the variability in CV_{V_f} for all of the latitudes decreases and tends to zero. The CV_{V_f} values for 45°N ranges from 0.1 to 1.0. Similar to the pattern observed for $CV_{\langle\theta\rangle} - \langle\theta\rangle$ for the different latitudes, the CV_{V_f} increases with an increase from the lower latitude (15°N) towards the higher latitude (45°N) due to the distribution of solar radiation. The least spatial variability is observed at 15°N, as the differences in incoming solar radiation on the NFS to the SFS are attenuated (Gerten, 2013; Gutiérrez-Jurado et al., 2013; Yetemen et al., 2015b).

Fig. 7c illustrates the results of $CV_{V_f} - \langle V_f\rangle$ for the four different K_{diff} scenarios, where K_{diff} = 0.0003 m^2/y displays the highest spatial variability in vegetation cover, with itsCV_{V_f} = 1.1, while the lowest CV_{V_f} occurs for K_{diff} = 0.015 m^2/y. There is a considerable difference between the value of CV_{V_f} for K_{diff} = 0.0003 m^2/y and that for the other hillslope diffusion cases (K_{diff} = 0.003, 0.009, 0.015 m^2/y) up to $\langle V_f\rangle$ = ~0.3. The CV_{V_f} difference diminishes after $\langle V_f\rangle$= ~0.3 for all of the four different K_{diff} cases. The high CV_{V_f} for 0.0003 m^2/y can be attributed to the landscape shape (shown in Fig. 2), which is dominated by fluvial erosion processes that lead to higher drainage density. Diffusive erosion processes, on the other hand, which are dominant for K_{diff} = 0.015 m^2/y, lead to low CV_{V_f}. It is noteworthy that fluvial erosion-dominated landscapes exhibit lower drainage areas and relatively higher spatial variability compared to other landscapes. Consequently, these landscapes showcase a greater degree of heterogeneity in vegetation cover. The interplay between landscape characteristics, erosion processes, and drainage patterns gives rise to this varibaility.

Regarding uplift rates effects (Fig. 7d), the high uplift rate (0.1 mm/y) is associated with higher CV_{V_f} compared to the other uplift cases of 0.05 mm/y and no uplift. The highest value (CV_{V_f} = ~0.8) is observed for the high uplift case, while the no uplift case exhibits considerably lower variation in the $CV_{V_f} - \langle V_f\rangle$ pattern than the other two cases. The CV_{V_f} increases for low $\langle V_f\rangle$ (~0.1) and gets attenuated for high $\langle V_f\rangle$. This can be attributed to the fact that uplift is a function of topographic steepness, and as uplift increases, the mean elevation of the topography increases (Tucker et al., 2001).

Results for the six MAP scenarios ranging from 200 mm to 600 mm (Fig. 7e) show that CV_{V_f} increases with MAP. In contrast, no significant variations can be observed in the $CV_{V_f} - \langle V_f\rangle$ relation for the elevation control MAP scenarios considered in Fig. 7f (for latitude 34°N). As seen in the remaining figures, changes in anisotropy ratio, root zone depth, porosity, infiltration capacity, and pore-size distribution lead to no significant changes in the $CV_{V_f} - \langle V_f\rangle$ plots (as shown in Fig. 7g–k the dots for different values of the parameters depicted in each sub-figure are either very similar or undistinguishable).

4.3. Impact of geomorphic factors on temporal variability of soil moisture and vegetation

The results and analysis presented in this section were designed to further explore the impact of geomorphic factors on soil moisture and vegetation variability. In addition to the previous results and to capture the variability of the soil moisture in space (including areas with different aspects), as explained in section 3.3, the mean temporal soil moisture, $\overline{\theta}$, and the mean temporal vegetation cover, $\overline{V_f}$, are computed for each pixel over the entire period and organized into mean temporal soil moisture-area and mean temporal vegetation cover-area plots. In

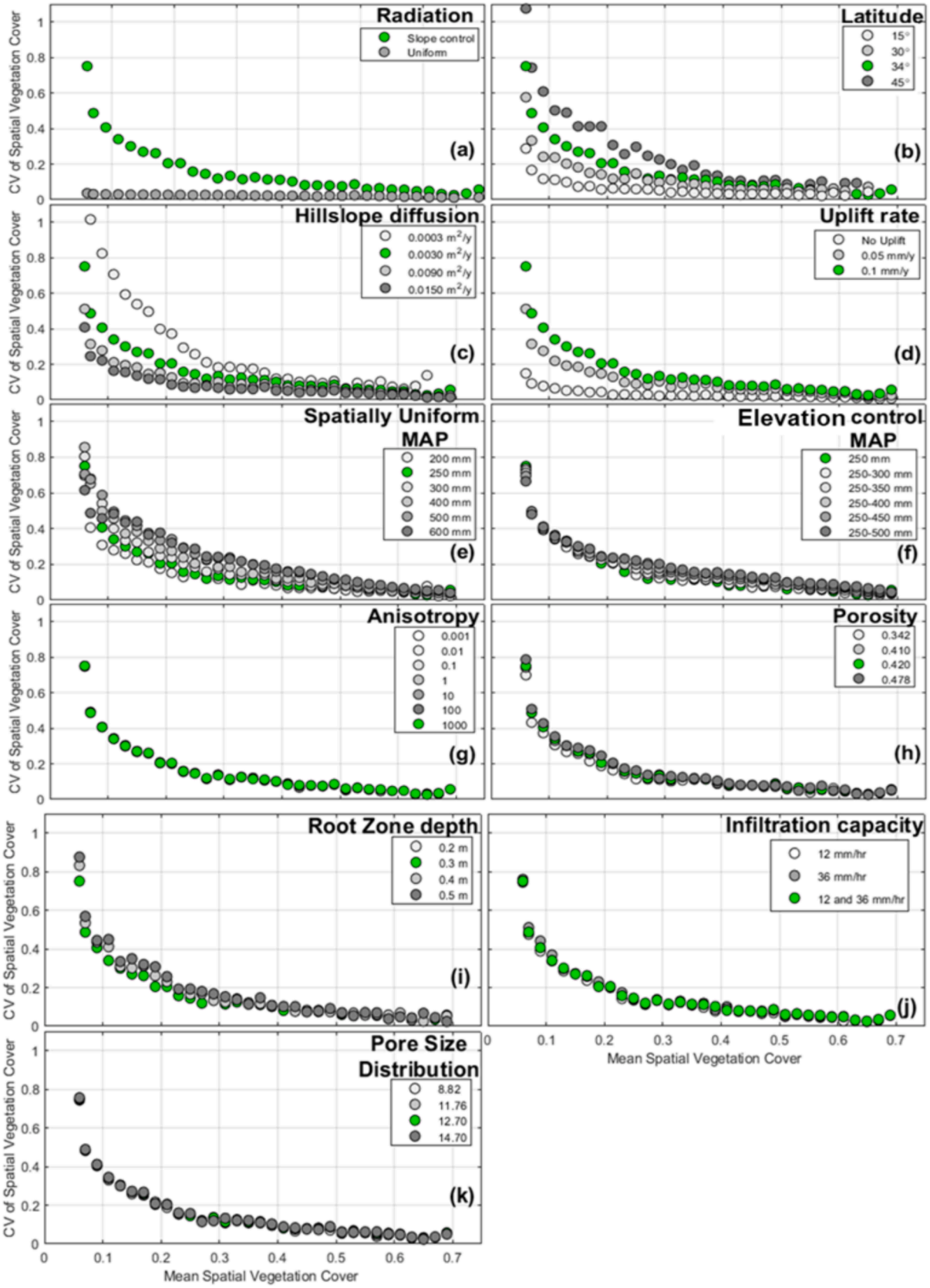

Fig. 7. Coefficient of the spatial variation of vegetation cover, CV_{V_f}, plotted as a function of spatial mean soil moisture, $\langle V_f \rangle$, over the entire domain for the eleven different soil moisture controlling factors (a–k). These $\langle V_f \rangle$ results for each time step are binned and plotted against CV_{V_f}. Green symbols represent the simulations for the control scenario detailed in Table 1. (For interpretation of the references to colour in this figure legend, the reader is referred to the web version of this article.)

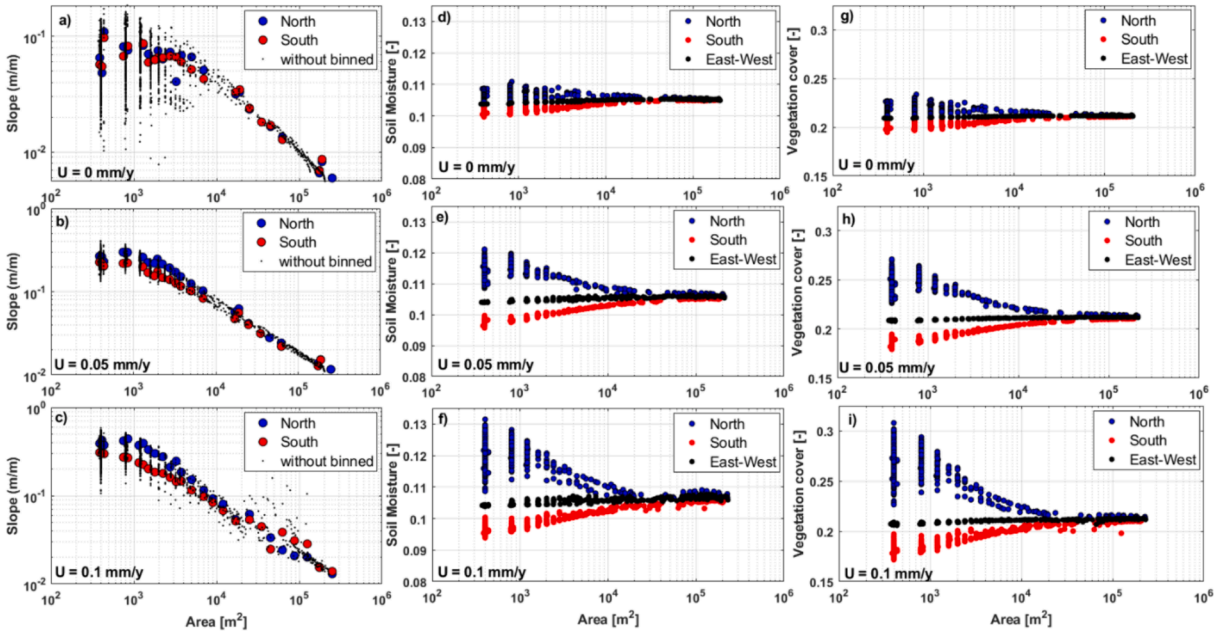

Fig. 8. Slope-area (first column), mean temporal soil moisture-area ($\bar{\theta}$, second column), and mean temporal vegetation-area ($\overline{V_f}$, third column) plotted for the NFS and SFS for the three different uplift cases (0, 0.05, and 0.1 mm/y). The blue dots represent values for the NFS and the red dots depict values for the SFS in all the plots. Note that the black dots in the slope-area represent all values of slope without binning, whereas they represent values for the east- and west-facing hillslopes in the soil moisture-area and vegetation-area plots. (For interpretation of the references to colour in this figure legend, the reader is referred to the web version of this article.)

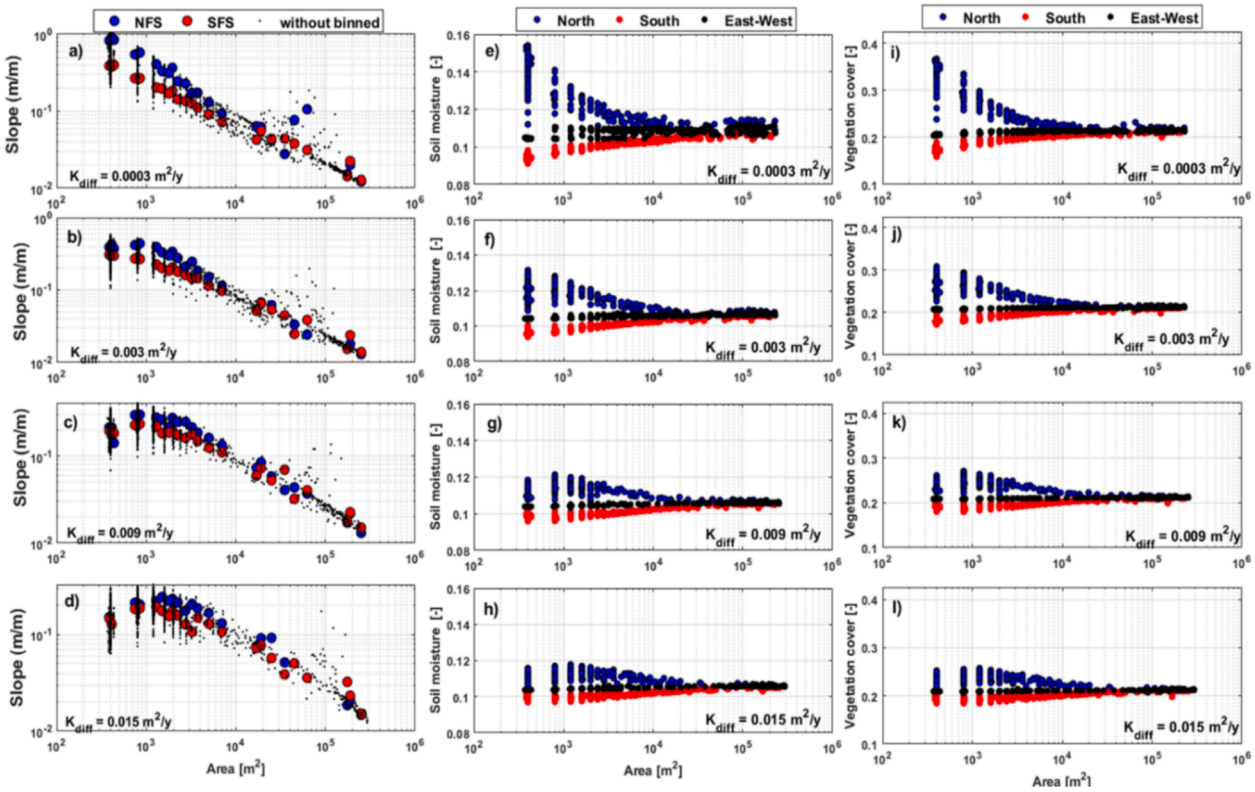

Fig. 9. Slope-area (first column), mean temporal soil moisture-area ($\bar{\theta}$, second column), and mean temporal vegetation-area ($\overline{V_f}$, third column) plotted for the NFS and SFS for four different hillslope diffusivity cases (K_{diff} = 0.0003, 0.003, 0.009 and 0.015 m^2/y). The blue dots represent values for the NFS and the red dots depict values for the SFS in all the plots. Note that the black dots in the slope-area represent all values of slope without binning, whereas they represent values for the east- and west-facing hillslopes in the soil moisture-area and vegetation-area plots. (For interpretation of the references to colour in this figure legend, the reader is referred to the web version of this article.)

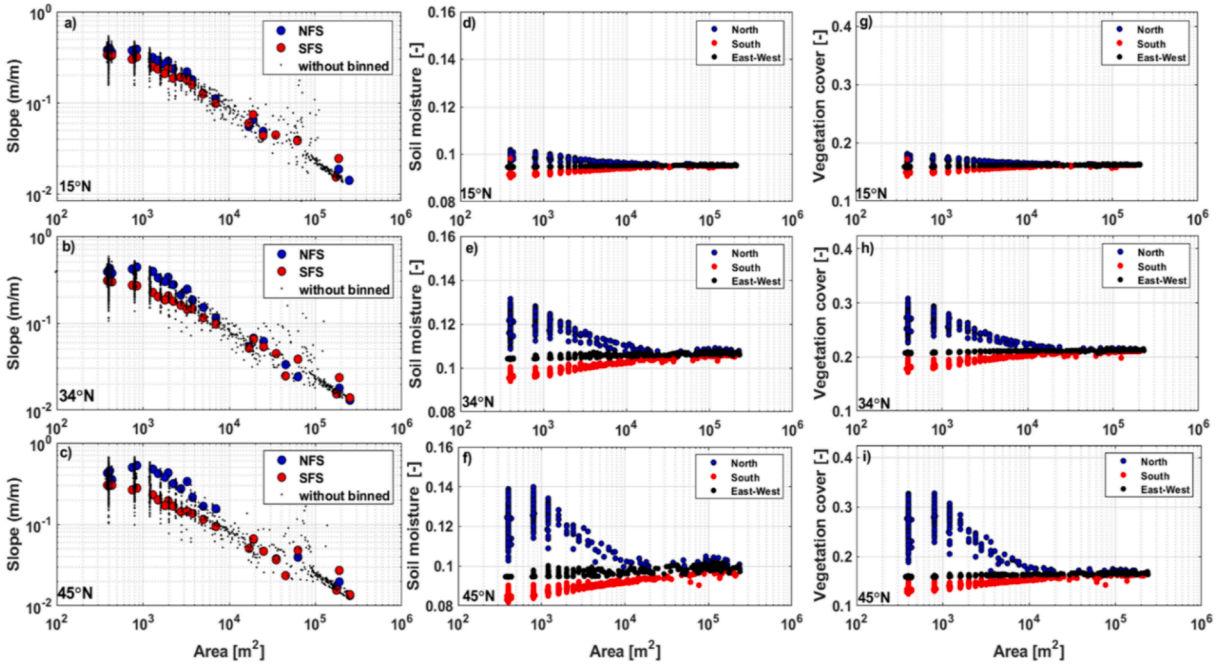

Fig. 10. Slope-area (first column), mean temporal soil moisture-area ($\overline{\theta}$, second column), and mean temporal vegetation-area ($\overline{V_f}$, third column) plotted for the NFS and SFS for the three latitude cases (i.e., 15°N, 30°N, and 45°N). The blue dots represent values for the NFS and the red dots depict values for the SFS in all the plots. Note that the black dots in the slope-area represent all values of slope without binning, whereas they represent values for the east- and west-facing hillslopes in the soil moisture-area and vegetation-area plots. (For interpretation of the references to colour in this figure legend, the reader is referred to the web version of this article.)

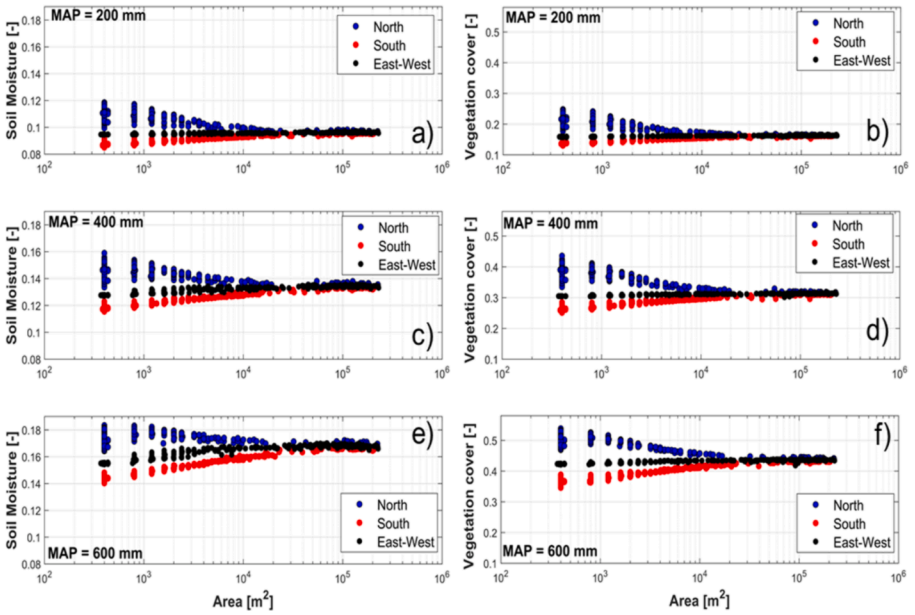

Fig. 11. Mean temporal soil moisture $\overline{\theta}$ and mean vegetation cover $\overline{V_f}$ plotted as a function of contributing drainage area without binning (showing all 1936 pixels) for four different aspects: north-, south-, east-, and west-facing slopes for the entire domain for 200, 400, and 600 mm MAP.

addition, slope-area (*S-A*) diagrams are used to visualise geomorphic process dominance over the topography.

Figs. 8-11 show the simulated values of slope (S), mean temporal soil moisture ($\overline{\theta}$), and mean temporal vegetation cover fraction ($\overline{V_f}$) plotted as a function of contributing drainage area (A) for different uplift rates, hillslope diffusion coefficients, latitudes, and MAP values, respectively. In order to capture the role of aspect (which critically affects evapotranspiration), each pixel is classified into four cardinal directions measured clockwise: North = 315°–360° and 0°–45°; East = 45°–135°; South = 135°–225°; and West = 225°–315°. The binned averages of S, $\overline{\theta}$, and $\overline{V_f}$ are calculated for pixels grouped into these four cardinal groups for the analysis and plots are presented below. It is important to note that the figures display the long-term temporal mean of soil moisture content ($\overline{\theta}$), whose values (0.095–0.16) are lower than the $\langle\theta\rangle$ values, which spans the range 0.060–0.33 (Fig. 5). Similarly, the range of values of $\overline{V_f}$ (0.17–0.38) are smaller than those of $\langle V_f\rangle$ (0.06–0.7) (Fig. 7). This

is due to the fact that $\langle\theta\rangle$ and $\langle V_f\rangle$ represent the spatial averages over the entire domain at each time step and capture the variability induced by seasonal differences in rainfall inputs, *PET* demand and ET_a over time, which is larger than the one induced by spatial soil moisture and vegetation distribution (at least over this relatively small domain).

Fig. 8a–c show two distinct features characteristics in the *S-A* diagrams. A slightly positive or negligible *S-A* gradient can be seen for A<~10^3 m^2 which corresponds to hillslopes with lower contributing areas where diffusion erosion processes are dominant. Thereafter, a negative *S-A* gradient can be observed for A>~10^3 m^2 where fluvial erosion processes become dominant. This result is consistent with the slope-area trends outlined in previous studies (Istanbulluoglu et al., 2008; Yetemen et al., 2010). Fig. 8d–f and 8 g–i show that a decreasing soil moisture and vegetation cover trend is observed for the NFS moving towards the outlet (increasing contributing drainage areas and decreasing slopes); while reverse trend (i.e., increasing mean soil moisture content and vegetation cover) is observed for the SFS as drainage area increases. With an increase in uplift rates the range in mean soil moisture and vegetation cover values also increase. The range of soil moisture values increases from 0.1 to 0.11 for U = 0 mm/y to ~ 0.095 to 0.134 for U = 0.1 mm/y. A similar increasing trend in the range of values is observed for vegetation cover, from ~ 0.19–0.23 for U = 0 mm/y to ~ 0.17 to 0.33 for U = 0.1 mm/y, respectively.

The difference in steepness between NFS and SFS increases for A<~10^4 m^2 and becomes more pronounced for higher uplift rates. This difference is reflected in the mean soil moisture (Fig. 8d–f) and the mean vegetation cover trends (Fig. 8g–i). As the slope steepens, the amount of solar radiation received on NFS during autumn and winter decreases, reducing PET and therefore enhancing soil moisture and vegetation cover. The SFS experience the opposite effect, that is, for steeper slopes the amount of solar radiation received during autumn and winter increases, increasing PET and decreasing soil moisture availability more than for the NFS. This difference in PET from incoming solar radiation creates considerable variation in $\overline{V_f}$ on the NFS and SFS. This finding in the current study is consistent with other field and modelling studies which show a higher rate of PET on SFS and a lower rate on NFS (McMahon, 1998; Bass et al., 2017; Yetemen et al., 2015a; Srivastava et al., 2021).

Regarding diffusivity dominance, the *S-A* plot for $K_{diff} = 0.0003$ m^2/y (Fig. 9a) shows that the negative trend between slope and contributing drainage extends to the entire range of contributing areas. In this case, the entire domain is dominated by fluvial processes, and the landscape has a wider range of soil moisture (~0.09 to 0.158; Fig. 9e) and vegetation cover (~0.15 – 0.36; Fig. 9i) compared with all of the other K_{diff} cases. This can be attributed to the higher drainage density of landscapes dominated by fluvial processes (as seen in Fig. 2). Fig. 9b for K_{diff} = 0.003 m^2/y, shows a slightly positive relationship in *S-A* (A<~10^3 m^2), which unlike the previous case, indicates the presence of erosion dominated by diffusion processes. From the figure, a negative gradient for A>~10^3 m^2 can also be observed, which shows the presence of fluvial erosion dominated processes as contributing area increases. Therefore, the landscape with $K_{diff} = 0.003$ m^2/y is having spatial areas in which one of the processes (diffusion or fluvial erosion) is dominant, which tends to reduce the range of mean temporal soil moisture (Fig. 9f) and mean temporal vegetation cover (Fig. 9j) variability as compared to the case with K_{diff} = 0.0003 m^2/y. The range of mean soil moisture values in this case varies from ~ 0.09 to 0.138, and mean vegetation cover varies from ~ 0.16 to 0.31. Fig. 9c–d show that as diffusion processes increase (as K_{diff} increases from 0.009 m^2/y to 0.015 m^2/y), the range of mean temporal soil moisture (Fig. 9g–h) and vegetation cover (Fig. 9k–l) continues to decrease. The range of mean temporal soil moisture decreases from ~ 0.009–0.12 for 0.009 m^2/y to ~ 0.09–0.11 for 0.015 m^2/y, respectively. A similar trend is observed for the vegetation cover for the 0.009 m^2/y and 0.015 m^2/y cases.

The plots in Fig. 10a–c show that as latitude increases (from 15°N towards 45°N), the difference between the gradient of the NFS and SFS tends to be more pronounced. The patterns of mean soil moisture and vegetation as a function of contributing area (Fig. 10d-f and 10 g-i) are overall similar to those depicted in Figs. 8-9.

The range of $\overline{\theta}$ values corresponding to the smaller drainage areas (~400 m^2) is wider for all of the latitudes, and decreases for higher drainage areas, showing that the role of aspect diminishes with increasing drainage area. In addition, when comparing the plots for increasing latitudes (from 15°N to 45°N), the range of values of $\overline{V_f}$ and $\overline{\theta}$ increases and the magnitude of vegetation cover on the NFS becomes larger compared with that on the SFS. The range of $\overline{V_f}$ at 15°N varies between 0.14 and 0.18 (Fig. 10g), which is lower than for 34°N (0.16–0.32; shown in Fig. 10*h*) and 45°N (0.16–0.33; shown in Fig. 10i). Higher latitudes increase the difference in incoming solar radiation on opposing hillslope aspects (Zou et al., 2007; Yetemen et al., 2015b); hence, the range of values of $\overline{V_f}$ and $\overline{\theta}$ are wider than for the lower latitudes.

As MAP increases from 200 to 600 mm, the range of mean soil moisture and vegetation cover widens (particularly for small contributing areas), and the difference in soil moisture magnitude between the NFS and SFS becomes larger (Fig. 11). The ranges of $\overline{\theta}$ and $\overline{V_f}$ for 200 mm vary between ~ 0.099–0.12 (Fig. 11a) and ~ 0.14–0.24 (Fig. 11b), respectively, which are lower than the corresponding ranges for 400 mm (i.e., ~0.11–0.16 (Fig. 11c) and 0.25–0.43 (Fig. 11d)). The ranges for $\overline{\theta}$ and $\overline{V_f}$ are the highest for 600 mm, varying between 0.14 and 0.19 (Fig. 11e) and 0.35–0.55 (Fig. 11f), respectively.

5. Conclusions

This study focuses on understanding soil moisture variability (SMV) and vegetation variability (VV) in both space and time within simulated coevolving landscapes in semiarid ecosystems obtained using a landscape evolution model coupled with an ecohydrological model (CHILD + BGM). In order to identify key controlling factors on SMV and VV we analyse a range of geomorphic, climatic and soil characteristics and parameters.

Solar radiation, latitude, hillslope diffusion, and uplift rate emerge as the most significant controls of spatial SMV and VV, while the other factors investigated (MAP, anisotropy, porosity, root zone depth, infiltration capacity and pore size distribution) lead to much lower impacts. For all cases analysed, the maximum spatial soil moisture variability occurred at intermediate values of the spatial average soil moisture, which is consistent with previous results (Srivastava et al. 2021, and references therein). The key role of aspect induced solar radiation on the spatial variability of both soil moisture and vegetation, is demonstrated as variability in simulations with slope-controlled solar radiation are remarkably higher than simulations those with uniform solar radiation (which show almost no variability). The impact of solar radiation is also highlighted by results from simulated landscapes at different latitudes, as the effect of solar radiation increases with latitude and is reflected by an increase in variability in both space and time (as explained in section 4.1), as higher latitudes amplify the difference in incoming solar radiation in opposing hillslope aspects (i.e., south versus north facing slopes).

In terms of geomorphic impacts, our study shows that landscapes generated under low uplift rates display less spatial variability than those under high uplift rates and that diffusive erosion dominated landscapes exhibit lower variability in soil moisture and vegetation cover than those in which fluvial erosion processes are prevalent, i.e., lower diffusivity (K_{diff}) values. These results are also linked to the effects of aspect-controlled solar radiation, as landscapes that coevolve to generate a steeper or more dissected topography tend to have more pronounced differences in solar radiation between south and north facing slopes, which leads to differences in soil moisture and vegetation cover.

This relation between high/low diffusivity and low/high variability in soil moisture is also highlighted by the analysis of time averaged spatial statistics (spatial averaged soil moisture, and spatial averaged variation coefficient), which indicates that landscapes with the same mean average soil moisture (determined by MAP and latitude) can display lower/higher spatiotemporal variability due to higher/lower diffusivity values.

The analysis of time averaged spatial statistics also reveals patterns of the effects of climatic factors (i.e., MAP and latitude). For a given value of diffusivity (K_{diff}) and uplift, the combination of MAP and latitude determines the values of mean average soils moisture and spatiotemporal variability. While the main effect of latitude is the increase in variability and the main effect of MAP is the increase in mean average soil moisture, combination of both effects can produce situations of higher soil moisture for a lower MAP in landscapes at mid-latitudes compared to those at the tropics.

Further confirmation of the effects of aspect-controlled radiation was obtained by analysing the slope-area diagrams and their relation to soil moisture and vegetation cover dynamics along hillslopes, showing the impact of topographic steepness and solar radiation distribution on these variables. We explored the influence of uplift rates, diffusivity, latitude and MAP on SMV and VV (in terms of variability of the time average values), revealing that the impacts on temporal variability in soil moisture and vegetation cover are more important for the smaller contributing areas (up to $2x10^4$ m^2) that have higher slopes (more than 10^{-1}), and are more pronounced in north than in south facing slopes. This phenomenon comes from the enhanced insolation difference between north and south facing slopes resulting from increased uplift rates, decreased diffusivity, increased latitude and increased MAP, thereby amplifying the SMV and VV dynamics. These findings resonate with existing field and modelling studies (McMahon, 1998; Bass et al., 2017; Yetemen et al., 2015a; Srivastava et al., 2021) that emphasise the higher rate of potential evapotranspiration on south facing slopes compared to north facing slopes.

There are several limitations in the current study as a result of the type of scenarios investigated and some of the model assumptions. Our scenarios do not include the effect of changes in relative humidity, air temperature and seasonality associated to changes in latitude. We have initially assumed that their effect on PET would be relatively homogeneous at the spatial scale analysed, but they can certainly vary with altitude even at small spatial scales, and therefore affect SMV and VV. Another limitation is that we do not consider the effect of snowfall. We have deliberately neglected latitudinal changes in temperature and precipitation in order to focus on model sensitivity to solar radiation, but future studies could explore the effects of snowfall on the results to enhance the accuracy and applicability of the findings.

In terms of model assumptions, our simulations consider spatially uniform soil hydraulic properties (e.g., porosity, soil texture), which may result in underestimation of SMV. Our model can underestimate SMV during wet periods when near saturation conditions tend to occur everywhere. In this situation the spatial variability of soil porosity will lead to (small) non-zero SMV that our simulations do not capture. Our model simulations also assume spatially uniform vegetation type and properties. In the current model setup grass is considered as the only vegetation type, which may result in underestimation of SMV, as different vegetation types with different phenology are likely to occur in slopes with different aspects.

Future efforts should be directed at incorporating more complex ecosystems such as shrublands and forests. Integration of multiple plant types and the inclusion of competition among tree, grass, and shrub vegetation will introduce new research avenues important to understanding regional water, sediment, and nutrient balances in semi-arid ecosystems.

These results highlight the significance of aspect-controlled differences in soil moisture and vegetation variability, which need to be accounted for in hydrology studies and the development of landscape indices (like the wetness and/or connectivity indices). These findings are very relevant for the parametrization of sub-grid soil moisture and vegetation variability in Earth System Models. They also have important implications for the verification of remotely sensed soil moisture and vegetation products.

CRediT authorship contribution statement

Ankur Srivastava: Conceptualization, Investigation, Methodology, Writing – original draft, Writing – review & editing. **Omer Yetemen:** Conceptualization, Investigation, Methodology, Writing – review & editing. **Jose F. Rodriguez:** Investigation, Methodology, Writing – review & editing. **Nikul Kumari:** Investigation, Methodology, Writing – original draft, Writing – review & editing. **Patricia M. Saco:** Conceptualization, Methodology, Writing – original draft, Writing – review & editing.

Declaration of competing interest

The authors declare that they have no known competing financial interests or personal relationships that could have appeared to influence the work reported in this paper.

Data availability

Data will be made available on request.

Acknowledgements

This research was funded by the University of Newcastle Postgraduate Research Scholarship (UNRSC) 50:50 (A. Srivastava). Additional funding was provided by the Australian Research Council through grants FT140100610 and DP140104178 (P.M. Saco) and the Scientific and Technological Research Council of Turkey (TUBITAK) through grant 118C329 (O. Yetemen).

Appendix A. Supplementary material

Supplementary data to this article can be found online at https://doi.org/10.1016/j.catena.2024.108125.

References

Anderson, R.S., Anderson, S.P., Tucker, G.E., 2013. Rock damage and regolith transport by frost: An example of climate modulation of the geomorphology of the critical zone. Earth Surf. Proc. Land. 38 (3), 299–316.

Baartman, J.E., Temme, A.J., Saco, P.M., 2018. The effect of landform variation on vegetation patterning and related sediment dynamics. Earth Surf. Proc. Land. 43 (10), 2121–2135.

Bass, B., Cardenas, M.B., Befus, K.M., 2017. Seasonal shifts in soil moisture throughout a semiarid hillslope ecotone during drought: A geoelectrical view. Vadose Zone J. 16 (2), 1–17.

Bhark, E.W., Small, E.E., 2003. Association between plant canopies and the spatial patterns of infiltration in shrubland and grassland of the Chihuahuan desert, New Mexico. Ecosystems 6 (2), 185–196.

Cabral, M.C., Garrote, L., Bras, R.L., Entekhabi, D., 1992. A kinematic model of infiltration and runoff generation in layered and sloped soils. Adv. Water Resour. 15, 311–324.

Carson, M.A., Kirkby, M.J., 1972. Hillslope form and process.

Casalini, A.I., Bouza, P.J., Bisigato, A.J., 2019. Geomorphology, soil and vegetation patterns in an arid ecotone. Catena 174 (November 2018), 353–361.

Caylor, K.K., Manfreda, S., Rodriguez-Iturbe, I., 2005. On the coupled geomorphological and ecohydrological organization of river basins. Adv. Water Resour. 28 (1), 69–86.

Chen, M., Willgoose, G.R., Saco, P.M., 201 Spatial prediction of temporal soil moisture dynamics using HYDRUS-1D. Hydrological Processes 28 (2), 171–185.

Clapp, R.B., Hornberger, G.M., 1978. Empirical equations for some soil hydraulic properties. Water Resour. Res. 14 (4), 601–660.

Collins, D.B.G., Bras, R.L., 2010. Climatic and ecological controls of equilibrium drainage density, relief, and channel concavity in dry lands. Water Resour. Res. 46, 1–18.

Dari, J., Morbidelli, R., Saltalippi, C., Massari, C., Brocca, L., 2019. Spatial-temporal variability of soil moisture: Addressing the monitoring at the catchment scale. J. Hydrol. 570 (January), 436–444.

Dethier, D.P., 2001. Pleistocene incision rates in the western United States calibrated using Lava Creek B tephra. Geology 29 (9), 783–786.
Detto, M., Montaldo, N., Albertson, J.D., Mancini, M., Katul, G., 2006. Soil moisture and vegetation controls on evapotranspiration in a heterogeneous Mediterranean ecosystem on Sardinia, Italy. Water Resour. Res. 42 (8), W08419.
Dietrich, W.E., Bellugi, D.G., Sklar, L.S., Stock, J.D., Heimsath, A.M., Roering, J.J., 2003. Geomorphic transport laws for predicting landscape form and dynamics. Geophys. Monogr. Ser. 135, 103–132.
Ding, J., Johnson, E.A., Martin, Y.E., 2018. Linking soil moisture variation and abundance of plants to geomorphic processes: A generalized model for erosion-uplifting landscapes. J. Geophys. Res. Biogeo. 123 (3), 960–975.
Dunne, T., Zhang, W.H., Aubry, B.F., 1991. Effects of rainfall, vegetation, and microtopography on infiltration and runoff. Water Resour. Res. 27 (9), 2271–2285.
Eagleson, P., 1978. Introduction to water balance dynamics. Water Resour. Res. 14 (5), 705–712.
Evaristo, J., Jasechko, S., McDonnell, J.J., 2015. Global separation of plant transpiration from groundwater and streamflow. Nature 525 (7567), 91–99.
Famiglietti, J.S., Rudnicki, J.W., Rodell, M., 1998. Variability in surface moisture content along a hillslope transect: Rattlesnake Hill, Texas. J. Hydrol. 210 (1–4), 259–281.
Famiglietti, J.S., Devereaux, J.A., Laymon, C.A., Tsegaye, T., Houser, P.R., Jackson, T.J., Van Oevelen, P.J., 1999. Ground-based investigation of soil moisture variability within remote sensing footprints during the Southern Great Plains 1997 (SGP97) Hydrology Experiment. Water Resour. Res. 35 (6), 1839–1851.
Famiglietti, J.S., Ryu, D., Berg, A.A., Rodell, M., Jackson, T.J., 2008. Field observations of soil moisture variability across scales. Water Resour. Res. 44 (1), 1–16.
Fan, K., Zhang, Q., Singh, V.P., Sun, P., Song, C., Zhu, X., Shen, Z., 2019. Spatiotemporal impact of soil moisture on air temperature across the Tibet Plateau. Sci. Total Environ. 649, 1338–1348.
Findell, K.L., Eltahir, E.A., 1997. An analysis of the soil moisture-rainfall feedback, based on direct observations from Illinois. Water Resour. Res. 33 (4), 725–735.
Geroy, I.J., Gribb, M.M., Marshall, H.P., Chandler, D.G., Benner, S.G., McNamara, J.P., 2011. Aspect influences on soil water retention and storage. Hydrol. Process. 25 (25), 3836–3842.
Gerten, D., 2013. A vital link: Water and vegetation in the Anthropocene. Hydrol. Earth Syst. Sci. 17 (10), 3841–3852.
Grayson, R.B., Western, A.W., Chiew, F.H.S., Blöschl, G., 1997. Preferred states in spatial soil moisture patterns: Local and nonlocal controls. Water Resour. Res. 33 (12), 2897–2908.
Gutiérrez-Jurado, H.A., Vivoni, E.R., Istanbulluoglu, E., Bras, R.L., 2007. Ecohydrological response to a geomorphically significant flood event in a semiarid catchment with contrasting ecosystems. Geophys. Res. Lett. 34 (24), 1–7.
Gutiérrez-Jurado, H.A., Vivoni, E.R., Cikoski, C., Harrison, J.B.J., Bras, R.L., Istanbulluoglu, E., 2013. On the observed ecohydrologic dynamics of a semiarid basin with aspect-delimited ecosystems. Water Resour. Res. 49 (12), 8263–8828.
Hack, J.T., Goodlett, J. C., 1960. Geomorphology and forest ecology of a mountain region in the central Appalachians (No. 347). United States Government Printing Office.
Hancock, G., Willgoose, G., 2001. Use of a landscape simulator in the validation of the SIBERIA catchment evolution model: Declining equilibrium landforms. Water Resour. Res. 37 (7), 1981–1992.
Hoekema, D.J., Sridhar, V., 2011. Relating climatic attributes and water resources allocation: A study using surface water supply and soil moisture indices in the Snake River basin, Idaho. Water Resour. Res. 47 (7).
Istanbulluoglu, E., Bras, R.L., 2005. Vegetation-modulated landscape evolution: Effects of vegetation on landscape processes, drainage density, and topography. Journal of Geophysical Research Earth Surface 110, 1–19.
Istanbulluoglu, E., Bras, R.L., 2006. On the dynamics of soil moisture, vegetation, and erosion: Implications of climate variability and change. Water Resour. Res. 42 (6), 1–17.
Istanbulluoglu, E., Wang, T., Wedin, D.A., 2012. Evaluation of ecohydrologic model parsimony at local and regional scales in a semi-arid grassland ecosystem. Ecohydrol. 5 (1), 121–142.
Ivanov, V.Y., Bras, R.L., Vivoni, E.R., 2008. Vegetation-hydrology dynamics in complex terrain of semiarid areas: 2. Energy-water controls of vegetation spatiotemporal dynamics and topographic niches of favorability. Water Resour. Res. 44 (3), 1–20.
Ivanov, V.Y., Fatichi, S., Jenerette, G.D., Espeleta, J.F., Troch, P.A., Huxman, T.E., 2010. Hysteresis of soil moisture spatial heterogeneity and the “homogenizing” effect of vegetation. Water Resour. Res. 46 (9), 1–15.
Kumari, N., Yetemen, O., Srivastava, A., Rodriguez, J. F., & Saco, P. M. (2019, December). The spatio-temporal NDVI analysis for two different Australian catchments. In Proceedings of the 23rd International Congress on Modeling and Simulation (MODSIM2019), Canberra, Australia (pp. 1-6).
Kumari, N., Saco, P.M., Rodriguez, J.F., Johnstone, S.A., Srivastava, A., Chun, K.P., Yetemen, O., 2020. The grass is not always greener on the other side: Seasonal reversal of vegetation greenness in aspect-driven semiarid ecosystems. Geophys. Res. Lett. 47 (15), e2020GL088918.
Laio, F., Porporato, A., Fernandez-Illescas, C.P., Rodriguez-Iturbe, I., 2001. Plants in water-controlled ecosystems: Active role in hydrologic processes and responce to water stress IV. Discussion of real cases. Adv. Water Resour. 24, 745–762.
Laursen, E.M., 1958. The total sediment load of streams. J. Hydraul. Div. Am. Soc. Civ. Eng. 84 (1530), 1–6.
Lee, T.J., 1992. The impact of vegetation on the atmospheric boundary layer and convective storms, doctoral thesis. Colorado State University, Fort Collins, Colorado.
Martinez, C., Hancock, G.R., Kalma, J.D., Wells, T., 2008. Spatio-temporal distribution of near-surface and root zone soil moisture at the catchment scale. Hydrological Processes: An International Journal 22 (14), 2699–271.
McMahon, D.R., 1998. Soil, landscape and vegetation interactions in small semi-arid drainage basin: Sevilleta National Wildlife Refuge, New Mexico, NMTech, Socorro, NM.
Meyer-Peter, E., Müller, R., 1948. Formulas for bed load transport, in Proc. of the 2nd Meeting of the International Association for Hydraulic Structures Research, pp. 39–64, International Association for Hydraulic Structures Research, Stockholm, Sweden.
Nearing, M.A., Simanton, J.R., Norton, L.D., Bulygin, S.J., Stone, J., 1999. Soil erosion by surface water flow on a stony, semiarid hillslope. Earth Surf. Proc. Land. 24 (8), 677–686.
Nearing, M.A., Unkrich, C.L., Goodrich, D.C., Nichols, M.H., Keefer, T.O., 2015. Temporal and elevation trends in rainfall erosivity on a 149 km2 watershed in a semi-arid region of the American Southwest. Int. Soil Water Conserv. Res. 3 (2), 77–85.
Nyberg, L., 1996. Spatial variability of soil water content in the covered catchment at Gårdsjön, Sweden. Hydrol. Process. 10 (1), 89–103.
Osborn, H.B., 198 Estimating precipitation in mountainous regions. J. Hydraul. Eng. 110 (12), 1859–1863.
Pan, Y.X., Wang, X.P., 2009. Factors controlling the spatial variability of surface soil moisture within revegetated-stabilized desert ecosystems of the Tengger Desert, Northern China. Hydrol. Process.: Int. J. 23 (11), 1591–1601.
Perera, H., Willgoose, G., 1998. A physical explanation of the cumulative area distribution curve. Water Resour. Res. 34 (5), 1335–1343.
Pielke, R.A., Avissar, R., Raupach, M., Dolman, A.J., Zeng, X., Denning, A.S., 1998. Interactions between the atmosphere and terrestrial ecosystems: Influence on weather and climate. Glob. Chang. Biol. 4 (5), 461–475.
Reynolds, J.F., Stafford Smith, D.M., Lambin, E.F., Turner, B.L., Mortimore, M., Batterbury, S.P.J., et al., 2007. Ecology: Global desertification: Building a science for dryland development. Science 316 (5826), 847–851.
Roering, J.J., Kirchner, J.W., Dietrich, W.E., 1999. Evidence for nonlinear, diffusive sediment transport on hillslopes and implications for landscape morphology. Water Resour. Res. 35 (3), 853–870.
Rossi, M.J., Ares, J.O., Jobbágy, E.G., Vivoni, E.R., Vervoort, R.W., Schreiner-McGraw, A. P., Saco, P.M., 2018. Vegetation and terrain drivers of infiltration depth along a semiarid hillslope. Sci. Total Environ. 644, 1399–1408.
Ryu, D., Famiglietti, J.S., 2005. Characterization of footprint-scale surface soil moisture variability using Gaussian and beta distribution functions during the Southern Great Plains 1997 (SGP97) hydrology experiment. Water Resour. Res. 41 (12), 1–13.
Saco, P.M., Moreno-de las Heras, M., 2013. Ecogeomorphic coevolution of semiarid hillslopes: Emergence of banded and striped vegetation patterns through interaction of biotic and abiotic processes. Water Resour. Res. 49 (1), 115–126.
Sehgal, V., Sridhar, V., 2019. Watershed-scale retrospective drought analysis and seasonal forecasting using multi-layer, high-resolution simulated soil moisture for Southeastern US. Weather Clim. Extremes 23, 100191.
Seneviratne, S.I., Corti, T., Davin, E.L., Hirschi, M., Jaeger, E.B., Lehner, I., et al., 2010. Investigating soil moisture-climate interactions in a changing climate: A review. Earth Sci. Rev. 99 (3–4), 125–161.
Small, E.E., 2005. Climatic controls on diffuse groundwater recharge in semiarid environments of the southwestern United States. Water Resour. Res. 41 (4), 1–17.
Sridhar, V., Hubbard, K.G., Wedin, D.A., 2006. Assessment of soil moisture dynamics of the Nebraska Sandhills using long-term measurements and a hydrology model. J. Irrig. Drain. Eng. 132 (5), 463–473.
Srivastava A, Yetemen O, Kumari N, Saco PM. 2019. Aspect-controlled spatial and temporal soil moisture patterns across three different latitudes. In Proceedings of the 23rd International Congress on Modeling and Simulation (MODSIM2019), Canberra, Australia; 979–985.
Srivastava, A., Kumari, N., Maza, M., 2020. Hydrological response to agricultural land use heterogeneity using variable infiltration capacity model. Water Resour. Manag. 34 (12), 3779–3794.
Srivastava, A., Saco, P.M., Rodriguez, J.F., Kumari, N., Chun, K.P., Yetemen, O., 2021. The role of landscape morphology on soil moisture variability in semi-arid ecosystems. Hydrol. Process. 35 (1), e13990.
Srivastava, A., Rodriguez, J.F., Saco, P.M., Kumari, N., Yetemen, O., 2021. Global analysis of atmospheric transmissivity using cloud cover, aridity and flux network datasets. Remote Sens. (Basel) 13 (9), 1716.
Srivastava, A., Yetemen, O., Saco, P.M., Rodriguez, J.F., Kumari, N., Chun, K.P., 2022. Influence of orographic precipitation on coevolving landforms and vegetation in semi-arid ecosystems. Earth Surf. Proc. Land. 47 (12), 2846–2862.
Swenson, J.J., Waring, R.H., 2006. Modelled photosynthesis predicts woody plant richness at three geographic scales across the north-western United States. Glob. Ecol. Biogeogr. 15 (5), 470–485.
Teuling, A.J., Troch, P.A., 2005. Improved understanding of soil moisture variability dynamics. Geophys. Res. Lett. 32 (5), 1.
Teuling, A.J., Seneviratne, S.I., Williams, C., Troch, P.A., 2006. Observed timescales of evapotranspiration response to soil moisture. Geophys. Res. Lett. 33 (23), 1–5.
Thompson, S.E., Harman, C.J., Heine, P., Katul, G.G., 2010. Vegetation-infiltration relationships across climatic and soil type gradients. J. Geophys. Res. Biogeo. 115 (G2).
Tucker, G.E., Hancock, G.R., 2010. Modeling landscape evolution. Earth Surf. Proc. Land. 35 (1), 28–50.
Tucker, G., Lancaster, S., Gasparini, N., Bras, R., 2001. The Channel-Hillslope Integrated Landscape Development Model (CHILD). Springer, Boston, MA.
van Genuchten, M.T., 1980. A closed-form equation for predicting the hydraulic conductivity of unsaturated soils. Soil Sci. Soc. Am. J. 44 (5), 892–898.

Vereecken, H., Kamai, T., Harter, T., Kasteel, R., Hopmans, J., Vanderborght, J., 2007. Explaining soil moisture variability as a function of mean soil moisture: A stochastic unsaturated flow perspective. Geophys. Res. Lett. 34 (22), 1–6.

Vinnikov, K.Y., Robock, A., Speranskaya, N.A., Schlosser, C.A., 1996. Scales of temporal and spatial variability of midlatitude soil moisture. J. Geophys. Res. Atmos. 101 (D3), 7163–7717.

Wainwright, J., 2005. Climate and climatological variations in the Jornada Experimental Range and neighbouring areas of the US Southwest. Adv. Environ. Monit. Model 2, 39–110.

Wang, T., Liu, Q., Franz, T.E., Li, R., Lang, Y., Fiebrich, C.A., 2017. Spatial patterns of soil moisture from two regional monitoring networks in the United States. J. Hydrol. 552, 578–585.

West, N., Kirby, E., Bierman, P., Clarke, B.A., 201 Aspect-dependent variations in regolith creep revealed by meteoric 10Be. Geology 42, 507–510, 10.1130/g35357.1.

Western, A.W., Grayson, R.B., Bloschl, G., Wilson, D.J., 2003. Spatial variability of soil moisture and its implications for scaling. Scaling Methods Soil Phys. 119–142.

Yetemen, O., Istanbulluoglu, E., Vivoni, E.R., 2010. Geomorphology: The implications of geology, soils, and vegetation on landscape morphology: Inferences from semi-arid basins with complex vegetation patterns in Central New Mexico. Geomorphology 116 (3–4), 246–263.

Yetemen, O., Istanbulluoglu, E., Flores-Cervantes, J.H., Vivoni, E.R., Bras, R.L., 2015a. Ecohydrologic role of solar radiation on landscape evolution. Water Resour. Res. 51 (2), 1127–1157.

Yetemen, O., Istanbulluoglu, E., Duvall, A.R., 2015b. Solar radiation as a global driver of hillslope asymmetry: Insights from an ecogeomorphic landscape evolution model. Water Resour. Philos. Phenomenol. Res. 51 (12), 9843–9861.

Yetemen, O., Saco, P.M., Istanbulluoglu, E., 2019. Ecohydrology controls the geomorphic response to climate change. Geophys. Res. Lett. 46 (15), 8852–8861.